Planck intermediate results XXIII : Galactic plane emission components derived from Planck with ancillary data

Ade, P. A. R.

2015-08

Ade , P A R , Keihänen , E , Kurki-Suonio , H , Lähteenmäki , A , Suur-Uski , A-S , Valiviita , J & Planck Collaboration 2015 , ' Planck intermediate results XXIII : Galactic plane emission components derived from Planck with ancillary data ' , Astronomy & Astrophysics , vol. 580 , A13 . https://doi.org/10.1051/0004-6361/201424434

http://hdl.handle.net/10138/233354
https://doi.org/10.1051/0004-6361/201424434

publishedVersion

A&A 580, A13 (2015)
DOI: 10.1051/0004-6361/201424434

Astronomy & Astrophysics

Planck intermediate results

XXIII. Galactic plane emission components derived from *Planck* with ancillary data⋆

Planck Collaboration: P. A. R. Ade[80], N. Aghanim[54], M. I. R. Alves[54], M. Arnaud[66], M. Ashdown[63,6], F. Atrio-Barandela[17], J. Aumont[54], C. Baccigalupi[79], A. J. Banday[83,10], R. B. Barreiro[60], E. Battaner[85], K. Benabed[55,82], A. Benoit-Lévy[23,55,82], J.-P. Bernard[83,10], M. Bersanelli[32,46], P. Bielewicz[83,10,79], J. Bobin[66], A. Bonaldi[62], J. R. Bond[9], F. R. Bouchet[55,82], F. Boulanger[54], C. Burigana[45,30], J.-F. Cardoso[67,1,55], A. Catalano[68,65], A. Chamballu[66,14,54], H. C. Chiang[26,7], P. R. Christensen[76,35], D. L. Clements[52], S. Colombi[55,82], L. P. L. Colombo[22,61], C. Combet[68], F. Couchot[64], B. P. Crill[61,77], F. Cuttaia[45], L. Danese[79], R. D. Davies[62,⋆⋆], R. J. Davis[62], P. de Bernardis[31], A. de Rosa[45], G. de Zotti[41,79], J. Delabrouille[1], C. Dickinson[62], J. M. Diego[60], S. Donzelli[46], O. Doré[61,11], M. Douspis[54], X. Dupac[38], G. Efstathiou[57], T. A. Enßlin[71], H. K. Eriksen[58], F. Finelli[45,47], O. Forni[83,10], M. Frailis[43], E. Franceschi[45], S. Galeotta[43], K. Ganga[1], R. T. Génova-Santos[59], T. Ghosh[54], M. Giard[83,10], G. Giardino[39], Y. Giraud-Héraud[1], J. González-Nuevo[60,79], K. M. Górski[61,86], A. Gregorio[33,43,49], A. Gruppuso[45], F. K. Hansen[58], D. L. Harrison[57,63], S. Henrot-Versillé[64], D. Herranz[60], S. R. Hildebrandt[11], E. Hivon[55,82], M. Hobson[6], A. Hornstrup[15], W. Hovest[71], K. M. Huffenberger[24], A. H. Jaffe[52], T. R. Jaffe[83,10], W. C. Jones[26], E. Keihänen[25], R. Keskitalo[20,12], T. S. Kisner[70], R. Kneissl[37,8], J. Knoche[71], M. Kunz[16,54,3], H. Kurki-Suonio[25,40], G. Lagache[54], A. Lähteenmäki[2,40], J.-M. Lamarre[65], A. Lasenby[6,63], C. R. Lawrence[61], R. Leonardi[38], M. Liguori[29], P. B. Lilje[58], M. Linden-Vørnle[15], M. López-Caniego[60], P. M. Lubin[27], J. F. Macías-Pérez[68], D. Maino[32,46], N. Mandolesi[45,5,30], P. G. Martin[9], E. Martínez-González[60], S. Masi[31], M. Massardi[44], S. Matarrese[29], P. Mazzotta[34], P. R. Meinhold[27], A. Melchiorri[31,48], L. Mendes[38], A. Mennella[32,46], M. Migliaccio[57,63], S. Mitra[51,61], M.-A. Miville-Deschênes[54,9], A. Moneti[55], L. Montier[83,10], G. Morgante[45], D. Mortlock[52], D. Munshi[80], J. A. Murphy[75], P. Naselsky[76,35], F. Nati[31], P. Natoli[30,4,45], H. U. Nørgaard-Nielsen[15], F. Noviello[62], D. Novikov[52], I. Novikov[76], C. A. Oxborrow[15], L. Pagano[31,48], F. Pajot[54], R. Paladini[53], D. Paoletti[45,47], F. Pasian[43], T. J. Pearson[11,53], M. Peel[62], O. Perdereau[64], F. Perrotta[79], F. Piacentini[31], M. Piat[1], E. Pierpaoli[22], D. Pietrobon[61], S. Plaszczynski[64], E. Pointecouteau[83,10], G. Polenta[4,42], N. Ponthieu[54,50], L. Popa[56], G. W. Pratt[66], S. Prunet[55,82], J.-L. Puget[54], J. P. Rachen[19,71], W. T. Reach[84], R. Rebolo[59,13,36], W. Reich[73], M. Reinecke[71], M. Remazeilles[62,54,1], C. Renault[68], S. Ricciardi[45], T. Riller[71], I. Ristorcelli[83,10], G. Rocha[61,11], C. Rosset[1], G. Roudier[1,65,61], J. A. Rubiño-Martín[59,36], B. Rusholme[53], M. Sandri[45], G. Savini[78], D. Scott[21], L. D. Spencer[80], V. Stolyarov[6,63,81], A. W. Strong[72], D. Sutton[57,63], A.-S. Suur-Uski[25,40], J.-F. Sygnet[55], J. A. Tauber[39], D. Tavagnacco[43,33], L. Terenzi[45], C. T. Tibbs[53], L. Toffolatti[18,60], M. Tomasi[46], M. Tristram[64], M. Tucci[16,64], L. Valenziano[45], J. Valiviita[40,25,58], B. Van Tent[69], J. Varis[74], P. Vielva[60], F. Villa[45], L. A. Wade[61], B. D. Wandelt[55,82,28], R. Watson[62], D. Yvon[14], A. Zacchei[43], and A. Zonca[27]

(Affiliations can be found after the references)

Received 19 June 2014 / Accepted 24 May 2015

ABSTRACT

Planck data when combined with ancillary data provide a unique opportunity to separate the diffuse emission components of the inner Galaxy. The purpose of the paper is to elucidate the morphology of the various emission components in the strong star-formation region lying inside the solar radius and to clarify the relationship between the various components. The region of the Galactic plane covered is $l = 300° \rightarrow 0° \rightarrow 60°$ where star-formation is highest and the emission is strong enough to make meaningful component separation. The latitude widths in this longitude range lie between 1° and 2°, which correspond to FWHM z-widths of 100−200 pc at a typical distance of 6 kpc. The four emission components studied here are synchrotron, free-free, anomalous microwave emission (AME), and thermal (vibrational) dust emission. These components are identified by constructing spectral energy distributions (SEDs) at positions along the Galactic plane using the wide frequency coverage of *Planck* (28.4−857 GHz) in combination with low-frequency radio data at 0.408−2.3 GHz plus WMAP data at 23−94 GHz, along with far-infrared (FIR) data from COBE-DIRBE and IRAS. The free-free component is determined from radio recombination line (RRL) data. AME is found to be comparable in brightness to the free-free emission on the Galactic plane in the frequency range 20−40 GHz with a width in latitude similar to that of the thermal dust; it comprises 45 ± 1% of the total 28.4 GHz emission in the longitude range $l = 300° \rightarrow 0° \rightarrow 60°$. The free-free component is the narrowest, reflecting the fact that it is produced by current star-formation as traced by the narrow distribution of OB stars. It is the dominant emission on the plane between 60 and 100 GHz. RRLs from this ionized gas are used to assess its distance, leading to a free-free z-width of $FWHM \approx 100$ pc. The narrow synchrotron component has a low-frequency brightness spectral index $\beta_{\rm synch} \approx -2.7$ that is similar to the broad synchrotron component indicating that they are both populated by the cosmic ray electrons of the same spectral index. The width of this narrow synchrotron component is significantly larger than that of the other three components, suggesting that it is generated in an assembly of older supernova remnants that have expanded to sizes of order 150 pc in 3×10^5 yr; pulsars of a similar age have a similar spread in latitude. The thermal dust is identified in the SEDs with average parameters of $T_{\rm dust} = 20.4 \pm 0.4$ K, $\beta_{\rm FIR} = 1.94 \pm 0.03$ (>353 GHz), and $\beta_{\rm mm} = 1.67 \pm 0.02$ (<353 GHz). The latitude distributions of gamma-rays, CO, and the emission in high-frequency *Planck* bands have similar widths, showing that they are all indicators of the total gaseous matter on the plane in the inner Galaxy.

Key words. ISM: general – Galaxy: general – radiation mechanisms: general – radio continuum: ISM – submillimeter: ISM – Galaxy: disk

1. Introduction

At radio, millimetre, and far-infrared (FIR) wavelengths the emission from the interstellar medium (ISM) is generated by

⋆ Appendices are available in electronic form at http://www.aanda.org

⋆⋆ Corresponding author: R. D. Davies, Rodney.Davies@manchester.ac.uk

four distinct mechanisms. The three long-recognized components are the free-free emission from ionized gas (e.g., Dickinson et al. 2003), the synchrotron emission from relativistic electrons spiralling in the Galactic magnetic field (Rybicki & Lightman 1979), and thermal (vibrational) emission from large dust grains (Désert et al. 1990). Another component has been identified, namely the anomalous microwave emission (AME) correlated with dust and emitting in the frequency range 15−50 GHz. This emission has a peaked spectrum centred at 20−30 GHz and is believed to be electric dipole radiation from small spinning dust grains (Draine & Lazarian 1998a,b). A new flat-synchrotron component, the microwave haze, associated with gamma-ray emission, has also been identified at intermediate latitudes (Dobler et al. 2010; Planck Collaboration Int. IX 2013), but is not of concern here.

The aim of this paper is to study the inner Galaxy where the four emission components at radio and millimetre wavelengths peak in a narrow latitude band. In the past the components have been difficult to separate because their morphologies are similar, which is not the case at higher latitudes where component separation techniques have been successful (Gold et al. 2011; Planck Collaboration Int. XII 2013). The region $l = 300° \rightarrow 0° \rightarrow 60°$, $|b| < 2°$ is the most active star formation area in the Galaxy. The latitude- or z-width of a component reflects its recent history. The most recent (current) star formation may be traced in the distribution of the dense CO and CS molecular clouds. The free-free emission traces both the current OB stars in individual H II regions and the diffuse emission produced by the sum of all the ionizing stars. The narrow distribution of synchrotron emission traces the supernova remnants (SNRs) as they expand and become a diffuse background over their 10^5−10^6 yr lifetime. The latitude distribution of pulsars, which are also born in SN events, is also relevant to the discussion. The total gaseous mass distribution in latitude can be inferred from the thermal dust emission (Planck Collaboration XIX 2011) and the gamma-ray π_0-decay data (Grenier et al. 2005). We will show that it is possible to separate the narrow latitude distribution from the broad distribution in each of the four mechanisms, in emission from the Gould Belt system in which the Sun lies, in the local spiral arm, and in the Galactic halo.

There are a number of methods available for separating the four emission components at intermediate and high Galactic latitudes. These methods assume that the components have different distributions on the sky, and require templates for each component. The 408 MHz map of Haslam et al. (1982) is used for the synchrotron emission template, and the Hα maps (WHAM, Reynolds et al. 1998; SHASSA, Gaustad et al. 2001; VTSS, Dennison et al. 1998) are used for the free-free template. The FIR maps (IRAS, Miville-Deschênes & Lagache 2005; COBE-DIRBE, Hauser et al. 1998) are used as templates for the dust-correlated AME and the thermal dust. However, on the Galactic plane the four components have similar narrow latitude distributions and cannot be separated morphologically. Nevertheless, with a large frequency coverage it is possible to construct comprehensive spectral energy distributions (SEDs) along the Galactic plane and fit spectral models to them. This is where *Planck*[1] (Tauber et al. 2010; Planck Collaboration I 2011) with its wide frequency coverage from 28.4 to 857 GHz combined with radio and FIR data can throw new light on the four Galactic plane components.

We will now summarize what is known about each of the components as determined at intermediate latitudes, which may act as a guide to what may be expected on the Galactic plane.

The Galactic synchrotron emission is generated by relativistic cosmic ray electrons (CRE) spiralling in the Galactic magnetic field. They have their origin in supernova shocks following the collapse of massive stars. The relativistic electrons eventually escape from the expanding remnants into the thin disk and subsequently into the Galactic halo. The high-energy component of the cosmic rays escapes from the supernova site and collides with interstellar gas to produce gamma-rays by π_0-decay. Neutron stars (pulsars) can also be produced in the stellar collapse; they are a good indicator of the Galactic supernova rate. The spectral index of the synchrotron power spectrum, α, is directly related to the spectral index, δ, of the CRE energy spectrum by the relation $\alpha = 0.5 \times (\delta - 1)$ (Rohlfs & Wilson 2004). The equivalent relation for the synchrotron brightness spectral index is $\beta_{\rm synch} = 0.5 \times (\delta + 3)$ (where $T_{\rm b} \propto \nu^{\beta}$). Energy loss by radiation steepens the electron energy spectrum and accordingly the synchrotron spectrum also steepens at higher frequencies. The synchrotron brightness temperature spectral index at frequencies below ∼1 GHz at intermediate latitudes is found to lie in the range −2.5 to −2.7 (Lawson et al. 1987; Broadbent et al. 1989; Platania et al. 1998, 2003). However it steepens significantly by 23 GHz to values of −2.9 to −3.2 as measured from 408 MHz (Banday et al. 2003; Davies et al. 2006; Gold et al. 2011; Ghosh et al. 2012). The steepening must occur somewhere in the range 2−20 GHz (Dunkley et al. 2009a; Peel et al. 2011; Strong et al. 2011). At WMAP frequencies the spectral index is −3.0 at intermediate latitudes (Banday et al. 2003; Davies et al. 2006; Kogut et al. 2011).

The free-free emission arises from the ionized component of the ISM. This ionization is produced by OB stars recently formed in high-density regions; some of the emission comes from compact H II regions and some is from the diffuse medium excited by the interstellar radiation field. The spectral shape of the free-free emission is well defined (Bennett et al. 1992; Dickinson et al. 2003; Draine 2011). The brightness temperature spectral index is $\beta_{\rm ff} \approx -2.10$ at 1 GHz, and steepens to $\beta_{\rm ff} \approx -2.14$ at 100 GHz. Hα data provide a good template for free-free emission at intermediate and high Galactic latitudes, although even here a correction is required to account for absorption by interstellar dust, which varies depending on the distributions of dust and ionized ISM along the line of sight. A fraction of the Hα emission may be scattered from the dust and would not have associated radio emission (Mattila et al. 2007; Witt et al. 2010; Brandt & Draine 2012). This fraction lies in the range 14% for low-density dust regions to 50% in cirrus-dominated regions. A more direct determination of the free-free emission in dust-embedded H II features at intermediate Galactic latitudes can be made using radio recombination lines (RRLs). On the Galactic plane this is the only direct method of determining the free-free emission (Hart & Pedlar 1976; Lockman 1976; Alves et al. 2010, 2012). In order to convert the RRL measurements into free-free brightness temperature ($T_{\rm b}$), it is necessary to know the electron temperature, $T_{\rm e}$ (as $T_{\rm b} \propto T_{\rm e}^{1.1}$). The fall in $T_{\rm e}$ towards the Galactic centre seen in individual H II regions (Shaver et al. 1983; Paladini et al. 2004) also applies to the diffuse free-free emission (Alves et al. 2012). The *Planck* 70.4 and 100 GHz channels are dominated by free-free emission on the Galactic plane. We will compare the estimates of the free-free

[1] *Planck* (http://www.esa.int/Planck) is a project of the European Space Agency – ESA – with instruments provided by two scientific Consortia funded by ESA member states (in particular the lead countries: France and Italy) with contributions from NASA (USA), and telescope reflectors provided in a collaboration between ESA and a scientific Consortium led and funded by Denmark.

from the component separation methods with the direct RRL determination for the longitude range $l = 20°-44°$.

Anomalous microwave emission (AME) has been observed in numerous experiments operating in the frequency range 10−60 GHz and peaks at 20−40 GHz (Kogut et al. 1996; de Oliveira-Costa et al. 1999; Banday et al. 2003; Lagache 2003; Finkbeiner 2004; Davies et al. 2006; Miville-Deschênes et al. 2008; Ysard & Verstraete 2010; Gold et al. 2011). It is closely correlated with thermal emission from dust grains. Electric dipole radiation from small, rapidly rotating dust grains is thought to be responsible. Theoretical models predict a spectrum peaking typically in the range 10−60 GHz, depending on the properties of the dust grains and their environment (Draine & Lazarian 1998a,b; Ali-Haïmoud et al. 2009; Dobler et al. 2009; Ysard & Verstraete 2010; Hoang et al. 2011). The most compelling evidence for spinning dust grains comes from dedicated observations covering frequencies ranging from the gigahertz radio bands (e.g., COSMOSOMAS, Cosmic Background Imager, Very Small Array) through the millimetre bands of WMAP and *Planck* to the FIR of IRAS and COBE-DIRBE. The best-studied examples at present are the Perseus molecular cloud (Watson et al. 2005; Tibbs et al. 2010; Planck Collaboration XX 2011) and the ρ Ophiuchi photo-dissociation region (Casassus et al. 2008; Planck Collaboration XX 2011); in these cases the peak is at 25–30 GHz. AME has also been detected in dust clouds associated with H II regions although with a range of emissivities (Todorović et al. 2010; Planck Collaboration XX 2011; Planck Collaboration Int. XII 2013; Planck Collaboration Int. XV 2014). We will show that the narrow distribution of the total AME emission on the the Galactic plane arises from a range of physical environments that include the diffuse ionized medium, H II regions, molecular clouds, and dust clouds with a spread of grain properties.

The spectrum of thermal dust is comprised of a cooler large-grain component and a warmer small-grain component (Désert et al. 1990; Planck Collaboration XXIV 2011). The large grains are responsible for the Rayleigh-Jeans emission tail measured by *Planck* while the small grains are responsible for the emission seen at near-IR wavelengths (∼5−40 μm) and also produce AME (Planck Collaboration XXI 2011). The near-IR band also includes emission from polycyclic aromatic hydrocarbons (PAHs) that may also contribute to AME (Tielens 2008; Ysard & Verstraete 2010; Ysard et al. 2010). The PAH fraction is greatest in regions of highest gas and molecular surface density (Sandstrom et al. 2010). Characterizing the Rayleigh-Jeans dust emission in the *Planck* regime is critical for the present study since it extends into the free-free, synchrotron, and AME domains. It is generally modelled in terms of a dust temperature, $T_{\rm dust}$, and a spectral index, $\beta_{\rm dust}$, by fitting over a broad spectral range. This is discussed in more detail in Planck Collaboration XIX (2011) and Planck Collaboration XXIV (2011). Conditions on the Galactic plane could be rather different from those at intermediate and high latitudes where the median value of $T_{\rm dust}$ is 19.7 ± 1.4 K and $\beta_{\rm dust} = 1.62 \pm 0.10$ (Planck Collaboration XI 2014).

Sections 2 and 3 describe the *Planck* and ancillary data used in this paper. The analysis methods for component separation are discussed in Sect. 4; these include `FastMEM` and SEDs. Section 5 describes the separation of the narrow and broad latitude distributions in each emission component and quantifies the narrow component in terms of a Gaussian amplitude and FWHM latitude width. Section 6 gives a discussion of the results of the component separation and uses the relative latitude widths to help understand the physical processes that lead to the different observed widths. The conclusions are presented in Sect. 7.

2. *Planck* data

Planck (Tauber et al. 2010; Planck Collaboration I 2011) is the third generation space mission to measure the anisotropy of the cosmic microwave background (CMB). It observed the sky in nine frequency bands covering 28.4−857 GHz with high sensitivity and with angular resolution from 31′ to 5′. The Low Frequency Instrument (LFI; Mandolesi et al. 2010; Bersanelli et al. 2010; Mennella et al. 2011) covered the 28.4, 44.1, and 70.4 GHz bands with amplifiers cooled to 20 K. The High Frequency Instrument (HFI; Lamarre et al. 2010; Planck HFI Core Team 2011a) covered the 100, 143, 217, 353, 545, and 857 GHz bands with bolometers cooled to 0.1 K. Polarization was measured in all but the highest two bands (Leahy et al. 2010; Rosset et al. 2010). A combination of radiative cooling and three mechanical coolers produced the temperatures needed for the detectors and optics (Planck Collaboration II 2011). Two data processing centers (DPCs) check and calibrate the data and make maps of the sky (Planck HFI Core Team 2011b; Zacchei et al. 2011). *Planck*'s sensitivity, angular resolution, and frequency coverage make it a powerful instrument for Galactic and extragalactic astrophysics as well as cosmology. Early astrophysics results are given in Planck Collaboration VIII−XXVI 2011, based on data taken between 13 August 2009 and 7 June 2010. Intermediate astrophysics results are now being presented in a series of papers based on data taken between 13 August 2009 and 27 November 2010 (Planck Collaboration Int. IX 2013; Planck Collaboration Int. XII 2013; Planck Collaboration Int. XIV 2014; Planck Collaboration Int. XV 2014) and in the astrophysics papers from the 2013 cosmology results (Planck Collaboration I 2014; Planck Collaboration XI 2014; Planck Collaboration XIII 2014).

In this paper we use *Planck* data from the 2013 product release (Planck Collaboration I 2014) that are available from the *Planck* Legacy Archive.[2] The data were acquired by *Planck* during its "nominal" operations period from 13 August 2009 to 27 November 2010. Specifically, we use the nine temperature maps at nominal frequencies of 28.4, 44.1, 70.4, 100, 143, 217, 353, 545, and 857 GHz (see Table 1).

We assume Gaussian beams and use the average beamwidths given in Planck Collaboration I (2014). We note that, due to the smoothing applied here, details of the beam, such as the exact shape of the beam and its variation across the sky, do not significantly affect the results. Furthermore, extended emission is less sensitive to the details of the beam. We convert from CMB thermodynamic units to Rayleigh-Jeans brightness temperature units using the standard conversion factors given in Planck Collaboration (2013). Colour corrections to account for the finite bandpass at each frequency are applied during the modelling of each spectrum; these are typically 1−3% for LFI and 10−15% for HFI. The *Planck* bands centred at 100, 217, and 353 GHz are contaminated by Galactic CO lines. When determining SEDs for thermal dust we apply a CO correction (see Sect. 3.5).

3. Ancillary data

Although *Planck* observed over a wide frequency range (28.4−857 GHz), it is still important to include ancillary data to

[2] http://www.sciops.esa.int/index.php?project=planck\&page=Planck_Legacy_Archive

Table 1. Summary of the data.

Telescope/ survey	Frequency [GHz]	Angular resolution [arcmin]	Coverage	Notes
JB/Eff/Parkes[a]	0.408	51.′0	Full-sky	NCSA desourced/destriped version[b]
Stockert/Villa-Elisa[c]	1.420	35.′4	Full-sky	Courtesy of W. Reich
HartRAO[d]	2.326	20.′0	Southern sky	Courtesy of Jonas (priv. comm.)
WMAP 9-yr[e]	22.8	51.′3	Full-sky	1° smoothed version[b]
Planck LFI[f]	28.4	32.′3	Full-sky	
WMAP 9-yr[e]	33.0	39.′1	Full-sky	1° smoothed version[b]
WMAP 9-yr[e]	40.7	30.′8	Full-sky	1° smoothed version[b]
Planck LFI[f]	44.1	27.′1	Full-sky	
WMAP 9-yr[e]	60.7	21.′1	Full-sky	1° smoothed version[b]
Planck LFI[f]	70.4	13.′3	Full-sky	
WMAP 9-yr[e]	93.5	14.′8	Full-sky	1° smoothed version[b]
Planck HFI[f]	100	9.′7	Full-sky	
Planck HFI[f]	143	7.′3	Full-sky	
Planck HFI[f]	217	5.′0	Full-sky	
Planck HFI[f]	353	4.′8	Full-sky	
Planck HFI[f]	545	4.′7	Full-sky	
Planck HFI[f]	857	4.′3	Full-sky	
COBE-DIRBE[g]	1249	37.′1	Full-sky	LAMBDA website[b]
COBE-DIRBE[g]	2141	38.′0	Full-sky	LAMBDA website[b]
COBE-DIRBE[g]	2997	38.′6	Full-sky	LAMBDA website[b]
IRAS (IRIS)[h]	2997	4.′7	Near-full sky	
IRAS (IRIS)[h]	11988	3.′6	Near-full sky	
IRAS (IRIS)[h]	24975	3.′5	Near-full sky	
Planck HFI[i]	CO	9.′7	Full-sky	Type 1 MILCA version
Parkes[j]	RRL	∼15′	$l = 20°$–$44°$, $\|b\| \leq 4°$	
Fermi[k]	Gamma-ray	∼88′	Full-sky	Dobler et al. (2010)[l]
Arecibo/ATNF/GB-NRAO/JB[m]	Pulsars	...	Full-sky	ATNF Pulsar Catalogue[n]
Leiden/ Dwingeloo[o]	H I	∼30–60′	Full-sky	LAMBDA website[b]

References. [(a)] Haslam et al. (1982); [(b)] http://lambda.gsfc.nasa.gov/; [(c)] Reich (1982); [(d)] Jonas et al. (1998); [(e)] Bennett et al. (2013); [(f)] Planck Collaboration I (2014); [(g)] Hauser et al. (1998); [(h)] Miville-Deschênes & Lagache (2005); [(i)] Planck Collaboration XIII (2014); [(j)] Alves et al. (2012); [(k)] Atwood et al. (2009); [(l)] http://astrometry.fas.harvard.edu/skymaps/fermi/; [(m)] Manchester et al. (2005); [(n)] http://www.atnf.csiro.au/research/pulsar/psrcat; [(o)] Hartmann & Burton (1997), Dickey & Lockman (1990).

extend the frequency range into the FIR, and in particular, to lower frequencies. To supplement *Planck* data we therefore used a range of publicly available surveys and data available within the team (Table 1). In the following sections, we describe the various data sets in more detail. We used the most up-to-date versions of the data sets, and where necessary regridded the maps into the HEALPix format (Górski et al. 2005) by using a procedure that computes the surface intersection between individual pixels of the survey with the intersecting HEALPix pixels. This procedure has been shown to conserve photometry (Paradis et al. 2012). We note that there are significant baseline uncertainties (i.e., offsets) in these maps, but these will not affect our results since we are subtracting a broad component from the Galactic emission, which removes any such offset.

3.1. Low-frequency radio data

The radio data include the full-sky map at 408 MHz (Haslam et al. 1982), the full-sky map at 1420 MHz (Reich 1982; Reich & Reich 1986; Reich et al. 2001), and the 2326 MHz HartRAO southern survey (Jonas et al. 1998) (Table 1). For this work we used a raw version of the 408 MHz map[3] at 51′ resolution rather than the widely used National Center for Supercomputing Applications (NCSA) version. The NCSA map has been Fourier filtered to remove large-scale striations and as a result many bright sources have also been subtracted. Since we are considering the total emission in the narrow component, including both point sources and diffuse medium, we use the raw map reprojected to the HEALPix grid at $N_{\rm side} = 512$, which is then smoothed from 51′ to 1°. Striations are visible at intermediate latitudes; however they are less than ∼1% of the sky signal on the Galactic plane.

The 1420 MHz full-sky map was multiplied by a factor of 1.55 to account for the main beam to full beam ratio (Reich & Reich 1988). The formal uncertainty on calibration is 5%, but we increase this due to the beam conversion uncertainties. We assume a 10% overall calibration uncertainty for all these radio data sets as in Planck Collaboration Int. XV (2014).

3.2. WMAP data

WMAP 9-year data (Bennett et al. 2013) span 23−94 GHz and thus complement the *Planck* data, particularly the *K*-band (22.8 GHz) channel. We use the 1°-smoothed maps available from the LAMBDA website and we apply colour corrections to the central frequencies using the recipe of Bennett et al. (2013). We assume a conservative 3% overall calibration uncertainty.

[3] Available from the Lambda webpage: http://lambda.gsfc.nasa.gov/product/foreground/haslam_408.cfm

The results of using the standard WMAP 1°-smoothed maps and the deconvolved 1°-smoothed maps are within the uncertainties of each other.

3.3. COBE-DIRBE data

To sample the peak of the blackbody curve for temperatures $\gtrsim$15 K we include the COBE-DIRBE data at 240 μm (1249 GHz), 140 μm (2141 GHz), and 100 μm (2997 GHz). The COBE-DIRBE data are the Zodi-Subtracted Mission Average (ZSMA) maps (Hauser et al. 1998) regridded into the HEALPix format. Colour corrections were applied as described in the COBE-DIRBE explanatory supplement version 2.3. We assume a 13% overall calibration uncertainty.

3.4. IRIS data

The IRIS data (Miville-Deschênes & Lagache 2005) are the reprocessed versions of the original IRAS data. Colour corrections are applied as described in the COBE-DIRBE and IRAS explanatory supplements. We assume a 13% overall calibration uncertainty (Beichman et al. 1988).

3.5. CO data

We use the Type 1 modified independent linear combination algorithm (MILCA, Hurier et al. 2013) maps of the CO emission (Planck Collaboration XIII 2014) to derive the latitude and longitude distributions of CO $J = 1 \rightarrow 0$ at 100 GHz. There is an overall agreement of 16% across the whole sky between the composite survey of Dame et al. (2001) and the *Planck* Type 1 CO $J = 1 \rightarrow 0$ map. When determining SED estimates, we use the Type 1 MILCA CO maps at 100, 217, and 353 GHz, as in Planck Collaboration Int. XIV (2014). The intensities are accurate to 10%, 2%, and 5% at 100, 217, and 353 GHz respectively (Planck Collaboration XIII 2014).

3.6. RRL data

The RRL data from the H I Parkes All-Sky Survey are used as a measure of the free-free brightness temperature at 1.4 GHz (Alves et al. 2012). The map covering $l = 20°-44°$, $|b| \leq 4°$ is regridded into the HEALPix format ($N_{\rm side} = 512$) as described in the introduction of Sect. 3 and is in units of millikelvin (Rayleigh-Jeans). These data have an overall calibration uncertainty of 15% arising from systematic biases in the free-free estimate from the measured RRLs. These are due to the assumed electron temperature and to the different conversion factors of antenna to brightness temperature for point sources and for diffuse emission. These will be discussed further in Sect. 6.1.

3.7. Gamma-ray data

The most up-to-date information on the all-sky distribution of gamma-rays is from the *Fermi*-LAT, the Large Area Telescope on the *Fermi* Gamma-ray Space Telescope (Atwood et al. 2009), which covers the energy range 20 MeV to 300 GeV. The angular resolution depends strongly on energy. At 1 GeV the 68.6% containment angle is $\approx 0\overset{\circ}{.}8$ and varies as $\sim E^{-0.8}$ (Ackermann et al. 2012). *Fermi*-LAT is sensitive to four components of diffuse emission; (i) gamma-rays from cosmic rays interacting with all forms of interstellar gas through π_0-production; (ii) bremsstrahlung from cosmic ray electrons (CREs); (iii) inverse Compton (IC) scattering of soft interstellar photons by CREs; and (iv) the extragalactic isotropic emission. Above 10° in latitude and 1 GeV in energy, the extragalactic emission contributes about 20% of the total (Abdo et al. 2010c). In the Galactic plane the π_0-produced component dominates; the inverse compton (IC) emission amounts to 5−15% of the total diffuse emission depending on the energy (Ackermann et al. 2011).

In this study we use data from Dobler et al. (2010) in the energy range 0.5−1.0 GeV, which represent π_0-decay from the total matter distribution, although bremsstrahlung is also significant in this range. Point sources have not been masked and the resolution is 88′ FWHM. This width is used when deriving the intrinsic FWHM of the gamma-ray emission.

3.8. Pulsar data

The ATNF catalogue of ∼2000 pulsars (Manchester et al. 2005) contains all the spin-powered pulsars so far detected at radio frequencies and at soft X-ray and gamma-ray energies. The latter two classes include isolated neutron stars that are spinning down in a similar manner to ordinary pulsars (Lorimer et al. 2006; Keane & Kramer 2008). The pulsar properties of interest to the present work are the positions, distances, dispersion measures (DMs), and characteristic ages estimated from the observed spin-down rates. Most high-energy pulsars are young with ages $\lesssim 3 \times 10^5$ yr; they are concentrated on the Galactic plane and are most likely the counterparts of as-yet unidentified SNRs. Those associated with known SNRs have ages in the range 10^3-10^5 yr. By contrast, the millisecond pulsars are very old with ages up to 4×10^9 yr and are more widely distributed in Galactic latitude; they are not of concern in this paper. The pulsar data are uniformly surveyed from $l = 270° \rightarrow 0° \rightarrow 40°$; at $40° < l < 90°$ the survey sensitivity is lower. The latitude widths discussed in this paper refer to the region $l = 320° \rightarrow 0° \rightarrow 40°$ of the highest pulsar count sensitivity.

3.9. HI data

We use the composite H I map available from the LAMBDA website to trace the spatial distribution of the neutral gas. The survey of Hartmann & Burton (1997) samples the sky for declinations $\delta \geq -30°$ every $0\overset{\circ}{.}5$, and is complemented by the lower-resolution survey of Dickey & Lockman (1990) with 1° sampling. Thus the final resolution of the map is survey dependent. These data are given in units of H I column density, converted from velocity-integrated H I brightness by multiplying by the factor 1.8224×10^{18} K km s^{-1} cm^{-2}. On the Galactic plane this estimate of the H I surface integral will be an underestimate of up to 20% because of the significant optical depth of H I at low Galactic latitudes (Dickey et al. 2009; Kalberla & Kerp 2009).

4. Analysis methods

A first step is to smooth all the maps to a common resolution of 1° using HEALPix $N_{\rm side} = 512$ (Górski et al. 2005). This resolution was chosen in order to include significant data sets with resolutions of ∼50′ (see Table 1); these are 408 MHz (51′), WMAP K- and Ka-bands (49′, 40′), COBE-DIRBE (40′), and 0.5−1 GeV gamma-rays (∼88′).

The next step was to use a common algorithm for identifying the narrow component (1°–2° wide) at each frequency. This ensured that we were working with the emission from the inner Galaxy. The broad local arm and any halo emission were thereby removed. The procedure was to fit a second-order polynomial to the latitude ranges $b = -5°$ to $-2°$ and $b = +2°$ to $+5°$ and interpolate between $-2°$ and $+2°$. First, we estimated the error in the polynomial by propagating the root mean square (rms) uncertainty in the latitude profile measured at high latitudes ($|b| > 20°$), which was then added in quadrature to the remaining narrow component. A Gaussian fit to the narrow component provides an amplitude and FWHM that are used in the subsequent analysis. The calibration uncertainties of the various data sets given in Sect. 3 are added in quadrature to the Gaussian fit uncertainties for the amplitude error. In order to have a robust estimate of the uncertainties in the latitude width, we also included the difference found between a direct measure of the width at half maximum of the narrow component and the result from the Gaussian fit. This difference is typically $0\overset{\circ}{.}05$ and is included in the tables. The CMB contribution is small compared with the emission on the Galactic plane used in the current study. On a 1° scale the CMB is ≤0.1 mK whereas the Galactic emission is ∼2 mK at 60−100 GHz where the Galactic emission is weakest.

4.1. Component separation methods applied to the Galactic plane

Component separation is of particular relevance to the estimation of the free-free along the Galactic plane where RRL data are not available. As indicated above, an estimate of the free-free unlocks the route to the other components. We use `FastMEM` (Stolyarov et al. 2002, 2005; Hobson et al. 1998), which is a non-blind method that can be used to separate a number of components with known frequency dependence. It is a model-fitting multi-frequency technique that works in the Fourier or spherical harmonic domain. The technique uses a Bayesian approach to search for the most probable solution for components having known properties (spectral and beam transfer function). `FastMEM` produces the solution, along with errors, in the spectral domain. It is particularly suitable for regions of high signal-to-noise ratio such as the Galactic plane (Bennett et al. 2013). The results of a comparison of the `FastMEM` free-free estimates with those of WMAP MEM (Bennett et al. 2013) and the direct RRL free-free estimates for $l = 20°$–$44°$ are given in Sect. 6.1. A description of the `FastMEM` technique is given in Appendix A, along with a comparison of results from other codes and from RRLs.

4.2. SEDs along the plane

The multi-frequency data at a common resolution of 1° were used to construct SEDs over appropriate longitude intervals along the Galactic plane at $b = 0\overset{\circ}{.}0$. The units of intensity are MJy sr^{-1}. The various emission components were then identified. The RRL data were used to determine the free-free brightness temperature at each frequency with a well-determined spectral index. Where the RRL data were not available, results of `FastMEM` (see Sect. 5 and Appendix A) were used. The synchrotron component was determined from the 408 MHz data corrected for the free-free contribution. The thermal dust emission was estimated by fitting to the *Planck* HFI frequencies and to the IRAS data augmented by the COBE-DIRBE data. After subtracting these three components from the total emission at each frequency, the remainder was taken as the AME emission spectrum.

5. Identification of a narrow component

Figures 1 and 2 show the narrow, bright structure of the inner Galaxy at four characteristic frequencies at which the emission is dominated by just one of the four components considered in this paper. These are (a) the 408 MHz map of Haslam et al. (1982) that is largely synchrotron emission (Alves et al. 2010); (b) the 28.4 GHz map from *Planck*, which has the strongest AME emission; (c) the 70.4 GHz map from *Planck*, which is mainly free-free (Planck Collaboration XXI 2011); and (d) the 545 GHz map from *Planck*, which is entirely thermal emission from large dust grains.

A narrow component of emission, 1−2° wide in Galactic latitude, is seen in the longitude range $l = 270° \rightarrow 0° \rightarrow 90°$ at all frequencies from 408 MHz through *Planck* frequencies to the FIR and gamma-rays. This is the emission from the star-forming regions within the gas and dust of the inner Galaxy. The spiral arms of this most active star formation in the Galaxy are usually called the Norma-Scutum and the Carina-Sagittarius arms. Figure 3 shows the distribution of H II regions on the Galactic disk where star formation is occurring, based on the work of Paladini et al. (2004). In the present work we will concentrate on the longitude range $l = 300° \rightarrow 0° \rightarrow 60°$, which encompasses the main emission from the inner arms. We will not be considering in this study the 3 kpc expanding arm or the Cohen-Davies bar of the innermost Galaxy (Cohen & Davies 1976; Bania et al. 2010). We reiterate that the total emission in the narrow component being studied here includes "point" (unresolved) sources such as SNRs, H II regions, and dust clouds as well as the diffuse medium; the ratio of H II region point sources to diffuse emission is 20−30% on scales of ≃15′ (Alves et al. 2012).

The free-free emission measure (EM) is proportional to the square of the electron density whereas all the other emission components studied here are proportional to the density. The vertical (z) distribution of electron density (n_e) can be derived from pulsar DM data in cases where the pulsars have reliable distances. This distribution has a narrow and a broad component. The widely used NE2001 model (Cordes & Lazio 2002, 2003) has a narrow distribution of scale height 140 pc ($e^{-|z|/z_0}$ with $z_0 = 140$ pc; *FWHM* = 190 pc) and a broad component of scale height 950 pc (*FWHM* = 1320 pc). Using more recent pulsar data, Lorimer et al. (2006) find that the thickness of the broad component is twice this value. In an attempt to reconcile the DM and EM thickness data of the broad component, Berkhuijsen et al. (2006) introduced a clumpiness (filling) factor to the model that is a function of z. In a comprehensive study, Gaensler et al. (2008) find a broad component with a scale height 1830 pc and $n_0 = 0.14$ cm^{-3} and a mid-plane filling factor $f_0 = 0.04$ (Berkhuijsen et al. 2006; Gaensler et al. 2008; Schnitzeler 2012). Although we are dealing with the narrow component in this paper, the discussion about a filling factor is relevant to our comparison of latitude distributions. If the warm ISM were simply a uniform mix of ionized and neutral gas/dust with a Gaussian latitude distribution then the FWHM of the EM would be $2^{-1/2}$ (or 71%) that of the electron and the neutral gas distributions.

5.1. Latitude distribution

Here we concentrate on the narrow component of the latitude distribution that arises in the ISM and is an integral through the

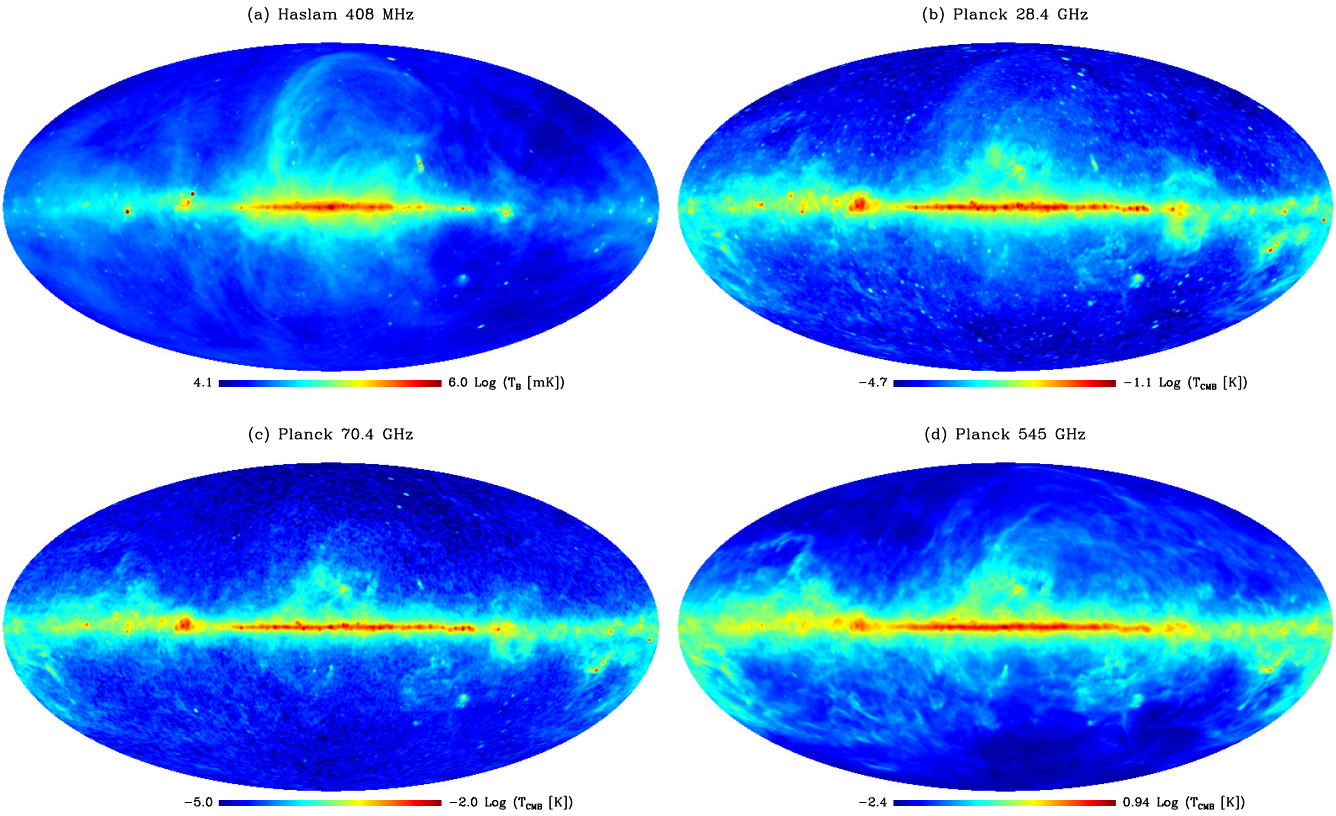

Fig. 1. Whole sky map at four frequencies showing the narrow inner Galaxy emission: **a)** the 408 MHz map of Haslam et al. (1982); **b)** the 28.4 GHz map from *Planck*; **c)** the 70.4 GHz map from *Planck*; and **d)** the 545 GHz map from *Planck*. The colour scales are logarithmic, and the maps are in Mollweide projection.

Galactic disk at ∼2−14 kpc from the Sun. The emission from the Local/Orion arm and the Gould Belt system in the longitude range being considered mostly arises within a distance of 0.5 kpc and produces a much broader and weaker signal that can be separated from the narrow innermost Galaxy emission. The results of this separation are illustrated in Fig. 4 for a range of frequencies with 1°-smoothed data averaged over the longitude range $l = 20°$ to 30°, which includes the Scutum and Sagittarius arms.

The 408 MHz amplitudes of the narrow and broad components of the inner Galaxy shown in Figs. 1a and 2a are similar. They are both closely confined to the region of high star formation in the range $l = 310° \rightarrow 0° \rightarrow 50°$. The FWHM of the narrow inner component is 1.°8, corresponding to a z-width of ∼180 pc at a typical distance of 6−8 kpc. The broad inner component has a FWHM of ∼10° corresponding to a z-width of 1−2 kpc, similar to the values given by Strong (2011) and Mertsch & Sarkar (2013). Lying outside this is a halo component ∼10 kpc in thickness (Phillipps et al. 1981; Beuermann et al. 1985; Strong 2011; Strong et al. 2011; Ghosh et al. 2012; Jaffe et al. 2011; Orlando & Strong 2013).

At *Planck* and IRAS frequencies the amplitude of the broad component is 9−15% of the narrow component. This broad component arises in the emission from the Gould Belt system within 500 pc of the Sun, and appears strongest at positive latitudes in the longitude range $l = 320° \rightarrow 0° \rightarrow 40°$ and at negative latitudes in the range 140°–220° (Perrot & Grenier 2003; Planck Collaboration Int. XII 2013). The CO and gamma-ray broad components have 12−20% of the amplitude of the narrow component, and are also associated with the northern Gould Belt system.

We now compare the latitude widths, with errors, of the various components in the longitude ranges $l = 320°$–340° and 20°–40° averaged in four 10° longitude intervals. Table 2 lists the observed FWHM at 1° resolution and the intrinsic FWHM obtained by deconvolving with a 1° Gaussian for each of the *Planck* bands. Ancillary data ranging from radio through FIR to gamma-rays are included. There are significant differences in the latitude widths in the different frequency bands. The low-frequency synchrotron emission is broadest. The bands associated with free-free are narrowest, while the dust emission is intermediate. These differences will be discussed in detail in Sect. 6.

A striking feature of Table 2 is the similarity in the widths of the emission bands in each of the longitude ranges $l = 330°-340°$, 20°−30°, and 30°−40°, while the widths at $l = 320°-330°$ are 1.35 times larger in each of the bands with a scatter of only 0.05 (at 95% confidence). This suggests that all four regions have similar emission properties, but the emitting region at $l = 320°-330°$ is closer.

5.2. Longitude distribution

We now turn to the longitude distribution of the data sets before studying the properties of each component.

The longitude distribution over the range $l = 270° \rightarrow 0° \rightarrow 90°$ at $b = 0°$ of the 1°-smoothed data is shown in Fig. 5 for selected frequencies: 408 MHz (mainly synchrotron), 28.4 GHz (mainly AME and free-free), 70.4 GHz (mainly free-free), 353 GHz (mainly dust), CO, gamma-rays, pulsars (representing supernovae), and 100 μm. Although each of the components represented is of a different origin, they have similar longitude distributions as a consequence of star formation in

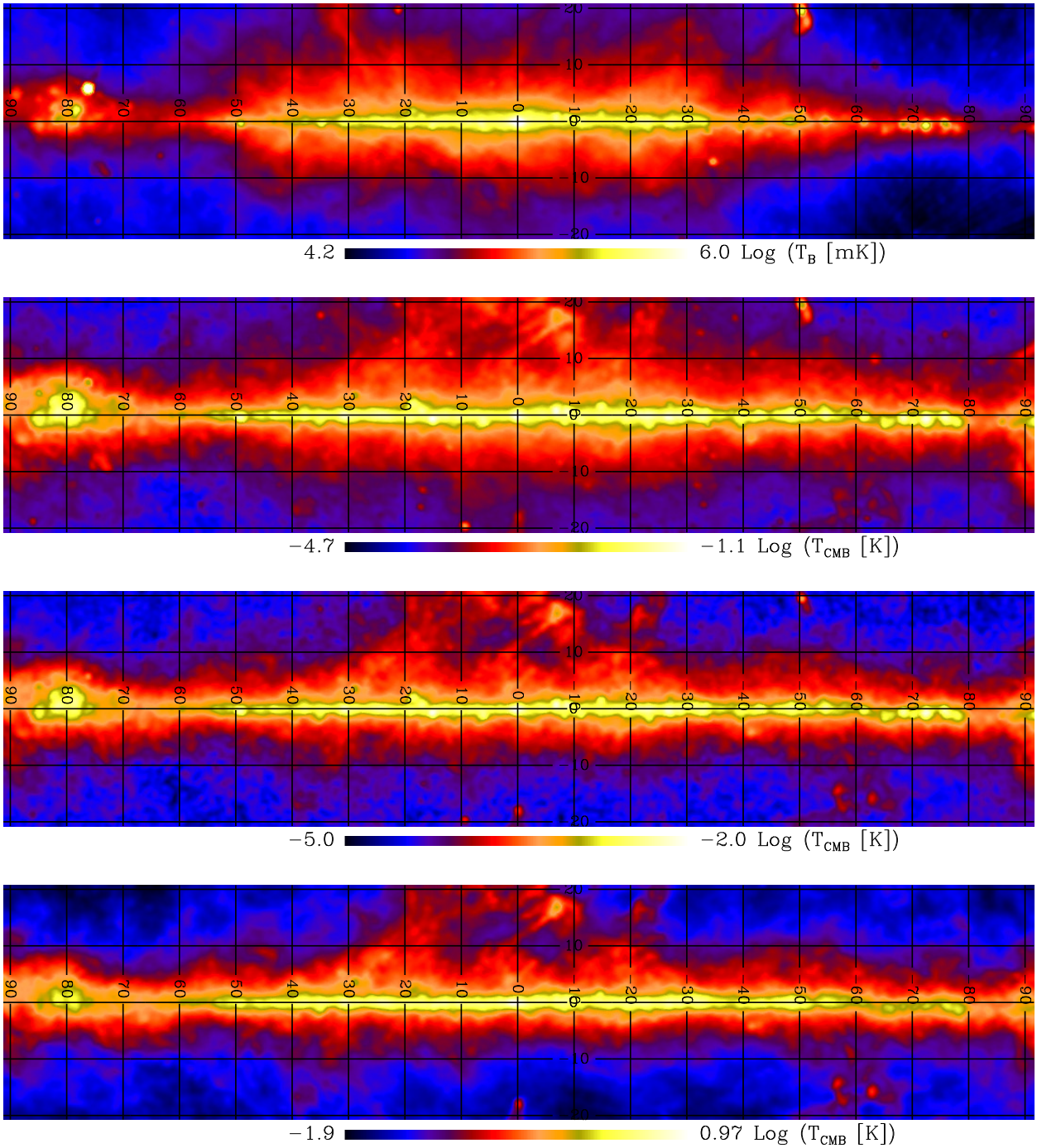

Fig. 2. Narrow Galactic emission at four frequencies: **a)** the 408 MHz map of Haslam et al. (1982); **b)** the 28.4 GHz map from *Planck*; **c)** the 70.4 GHz map from *Planck*; and **d)** the 545 GHz map from *Planck*. The colour scales are logarithmic. The longitude range is $l = 270° \rightarrow 0° \rightarrow 90°$; the latitude range is −20° to +20°. The maps are in Cartesian projection.

the regions of highest gas and dust density. Spiral arms can be identified through the longer emission length at their tangent points as seen from the Sun; the Carina arm tangent is seen at $l = 300°$, the Norma tangent at $l = 330°$, the Scutum tangent at $l = 25°$, and the Sagittarius tangent at $l = 45°$. These tangent points are at galactocentric distances of of 6.5, 4.5, 4.5, and 6.5 kpc respectively, assuming a solar galactocentric distance of 8.5 kpc (Clemens 1985).

Strong emission is seen in all the data sets in the longitude range $l = 357° \rightarrow 0° \rightarrow 3°$ around the Galactic centre, but we do not consider this region in the present study. Individual extended star-forming regions are seen in all the data sets, including Cygnus-X at $l = 80°$ and the Gum Nebula complex at $l = 286°$. More compact star-forming regions on a scale of 1° or less are seen at 408 MHz and the lower *Planck* frequencies at $l = 283°$, 287°, 306°, 328°, 31°, and 50°.

Table 2. Latitude widths and amplitudes of the narrow component in each band (*Planck* plus ancillary data) for the longitude ranges 20°–30°, 30°–40°, 320°–330°, and 330°–340°.

Data	*FWHM* (1° reso.)	*FWHM* (intrinsic)	Amplitude [mK]	*FWHM* (1° reso.)	*FWHM* (intrinsic)	Amplitude [mK]
	$l = 20°–30°$			$l = 30°–40°$		
0.408 GHz	1.°91 ± 0.°12	1.°63 ± 0.°14	(195 ± 20) × 10^3	1.°91 ± 0.°13	1.°63 ± 0.°16	(161 ± 17) × 10^3
1.4 GHz	1.°89 ± 0.°09	1.°60 ± 0.°11	(10.5 ± 1.1) × 10^3	1.°90 ± 0.°11	1.°61 ± 0.°13	(8.4 ± 0.8) × 10^3
2.3 GHz	1.°78 ± 0.°08	1.°47 ± 0.°10	(3.3 ± 0.3) × 10^3	1.°76 ± 0.°07	1.°45 ± 0.°09	(2.8 ± 0.3) × 10^3
RRL	1.°34 ± 0.°04	0.°90 ± 0.°06	(5.9 ± 0.6) × 10^3	1.°37 ± 0.°07	0.°93 ± 0.°10	(4.7 ± 0.5) × 10^3
23 GHz	1.°58 ± 0.°08	1.°22 ± 0.°10	35.3 ± 1.0	1.°61 ± 0.°11	1.°26 ± 0.°14	29.8 ± 0.9
28.4 GHz	1.°51 ± 0.°01	1.°14 ± 0.°01	22.0 ± 0.2	1.°55 ± 0.°04	1.°18 ± 0.°06	18.3 ± 0.2
33 GHz	1.°54 ± 0.°04	1.°18 ± 0.°06	15.5 ± 0.5	1.°57 ± 0.°07	1.°21 ± 0.°09	12.9 ± 0.4
41 GHz	1.°52 ± 0.°02	1.°14 ± 0.°03	9.2 ± 0.3	1.°55 ± 0.°05	1.°18 ± 0.°06	7.7 ± 0.2
44 GHz	1.°53 ± 0.°03	1.°16 ± 0.°04	7.52 ± 0.08	1.°56 ± 0.°06	1.°20 ± 0.°08	6.30 ± 0.06
60.7 GHz	1.°52 ± 0.°02	1.°15 ± 0.°03	3.7 ± 0.1	1.°57 ± 0.°07	1.°21 ± 0.°09	3.2 ± 0.1
70.4 GHz	1.°52 ± 0.°02	1.°15 ± 0.°03	2.93 ± 0.03	1.°59 ± 0.°09	1.°23 ± 0.°11	2.53 ± 0.03
94 GHz	1.°56 ± 0.°06	1.°19 ± 0.°07	2.37 ± 0.07	1.°66 ± 0.°06	1.°32 ± 0.°07	2.07 ± 0.07
100 GHz	1.°52 ± 0.°02	1.°14 ± 0.°03	2.2 ± 0.1	1.°63 ± 0.°03	1.°28 ± 0.°04	2.0 ± 0.1
143 GHz	1.°59 ± 0.°09	1.°24 ± 0.°12	2.73 ± 0.05	1.°75 ± 0.°14	1.°43 ± 0.°18	2.44 ± 0.05
217 GHz	1.°57 ± 0.°08	1.°21 ± 0.°09	4.77 ± 0.03	1.°72 ± 0.°12	1.°40 ± 0.°15	4.18 ± 0.02
353 GHz	1.°58 ± 0.°08	1.°22 ± 0.°10	8.7 ± 0.1	1.°73 ± 0.°13	1.°41 ± 0.°16	7.5 ± 0.1
545 GHz	1.°58 ± 0.°08	1.°22 ± 0.°10	15.0 ± 1.5	1.°72 ± 0.°12	1.°40 ± 0.°14	12.0 ± 1.2
857 GHz	1.°58 ± 0.°08	1.°23 ± 0.°11	24.0 ± 2.4	1.°69 ± 0.°09	1.°36 ± 0.°11	19.0 ± 1.9
1249 GHz	1.°57 ± 0.°07	1.°21 ± 0.°09	27.2 ± 3.5	1.°64 ± 0.°04	1.°30 ± 0.°05	20.9 ± 2.7
2141 GHz	1.°58 ± 0.°08	1.°23 ± 0.°11	16.0 ± 2.1	1.°62 ± 0.°02	1.°28 ± 0.°03	11.7 ± 1.5
2997 GHz	1.°59 ± 0.°09	1.°23 ± 0.°11	4.3 ± 0.6	1.°60 ± 0.°10	1.°25 ± 0.°13	3.0 ± 0.4
12 μm	1.°75 ± 0.°05	1.°44 ± 0.°06	(2.3 ± 0.3) × 10^{-3}	1.°75 ± 0.°05	1.°44 ± 0.°06	(1.5 ± 0.2) × 10^{-3}
CO	1.°48 ± 0.°08	1.°09 ± 0.°12	130 ± 13	1.°54 ± 0.°04	1.°17 ± 0.°05	91 ± 9
H I	1.°93 ± 0.°13	1.°65 ± 0.°15	(7.4 ± 0.7) × 10^3	2.°09 ± 0.°09	1.°84 ± 0.°10	(6.1 ± 0.6) × 10^3
Gamma-rays	1.°87 ± 0.°08	1.°18 ± 0.°11	(1.4 ± 0.1) × 10^{-4}	2.°00 ± 0.°10	1.°37 ± 0.°15	(1.1 ± 0.1) × 10^{-4}
Pulsar counts	1.°53 ± 0.°48	1.°15 ± 0.°63	15.1 ± 1.6	1.°58 ± 0.°45	1.°23 ± 0.°58	23.8 ± 3.5
	$l = 320°–330°$			$l = 330°–340°$		
0.408 GHz	2.°36 ± 0.°07	2.°14 ± 0.°08	(130 ± 13) × 10^3	1.°97 ± 0.°08	1.°70 ± 0.°09	(233 ± 23) × 10^3
1.4 GHz	2.°25 ± 0.°06	2.°02 ± 0.°07	(6.7 ± 0.7) × 10^3	1.°86 ± 0.°16	1.°57 ± 0.°19	(13.1 ± 1.3) × 10^3
2.3 GHz	2.°21 ± 0.°11	1.°97 ± 0.°12	(2.1 ± 0.2) × 10^3	1.°80 ± 0.°10	1.°50 ± 0.°12	(4.4 ± 0.4) × 10^3
23 GHz	1.°96 ± 0.°06	1.°68 ± 0.°07	22.4 ± 0.7	1.°60 ± 0.°10	1.°25 ± 0.°13	46.2 ± 1.4
28.4 GHz	1.°91 ± 0.°01	1.°63 ± 0.°01	13.66 ± 0.14	1.°54 ± 0.°04	1.°17 ± 0.°06	29.0 ± 0.3
33 GHz	1.°92 ± 0.°02	1.°64 ± 0.°03	9.7 ± 0.3	1.°57 ± 0.°07	1.°21 ± 0.°09	20.7 ± 0.6
41 GHz	1.°91 ± 0.°01	1.°63 ± 0.°01	5.82 ± 0.18	1.°55 ± 0.°05	1.°18 ± 0.°06	12.6 ± 0.4
44 GHz	1.°92 ± 0.°02	1.°64 ± 0.°02	4.80 ± 0.05	1.°56 ± 0.°06	1.°20 ± 0.°08	10.3 ± 0.1
60.7 GHz	1.°92 ± 0.°03	1.°64 ± 0.°03	2.50 ± 0.08	1.°55 ± 0.°05	1.°18 ± 0.°06	5.21 ± 0.16
70.4 GHz	1.°94 ± 0.°05	1.°67 ± 0.°05	2.01 ± 0.02	1.°55 ± 0.°05	1.°19 ± 0.°07	4.02 ± 0.04
94 GHz	1.°99 ± 0.°02	1.°72 ± 0.°02	1.70 ± 0.05	1.°59 ± 0.°09	1.°24 ± 0.°12	3.01 ± 0.09
100 GHz	2.°00 ± 0.°01	1.°72 ± 0.°02	1.74 ± 0.09	1.°60 ± 0.°01	1.°25 ± 0.°01	3.0 ± 0.1
143 GHz	2.°05 ± 0.°15	1.°79 ± 0.°17	2.07 ± 0.04	1.°65 ± 0.°05	1.°31 ± 0.°06	3.09 ± 0.06
217 GHz	2.°03 ± 0.°03	1.°77 ± 0.°04	3.52 ± 0.02	1.°64 ± 0.°04	1.°30 ± 0.°05	5.16 ± 0.04
353 GHz	2.°03 ± 0.°03	1.°77 ± 0.°04	6.33 ± 0.08	1.°64 ± 0.°04	1.°30 ± 0.°05	9.3 ± 0.1
545 GHz	2.°03 ± 0.°03	1.°76 ± 0.°03	10.0 ± 1.0	1.°64 ± 0.°14	1.°30 ± 0.°17	16.0 ± 1.6
857 GHz	2.°01 ± 0.°01	1.°75 ± 0.°02	15.0 ± 1.5	1.°64 ± 0.°14	1.°29 ± 0.°17	24.0 ± 2.4
1249 GHz	1.°98 ± 0.°02	1.°71 ± 0.°02	16.4 ± 2.1	1.°60 ± 0.°10	1.°26 ± 0.°13	28 ± 4
2141 GHz	1.°96 ± 0.°06	1.°69 ± 0.°07	8.8 ± 1.1	1.°60 ± 0.°01	1.°26 ± 0.°01	17 ± 2
2997 GHz	1.°93 ± 0.°03	1.°66 ± 0.°04	2.2 ± 0.3	1.°58 ± 0.°02	1.°23 ± 0.°02	4.7 ± 0.6
12 μm	2.°08 ± 0.°08	1.°83 ± 0.°09	(1.0 ± 0.1) × 10^{-3}	1.°76 ± 0.°04	1.°45 ± 0.°05	(2.1 ± 0.3) × 10^{-3}
CO	1.°97 ± 0.°03	1.°70 ± 0.°03	75 ± 8	1.°61 ± 0.°01	1.°26 ± 0.°01	108 ± 11
H I	2.°41 ± 0.°01	2.°19 ± 0.°01	(7.1 ± 0.7) × 10^3	2.°29 ± 0.°01	2.°06 ± 0.°01	(7.6 ± 0.8) × 10^3
Gamma-rays	2.°28 ± 0.°08	1.°75 ± 0.°11	(0.76 ± 0.08) × 10^{-4}	1.°91 ± 0.°11	1.°22 ± 0.°17	(1.27 ± 0.13) × 10^{-4}
Pulsar counts	1.°52 ± 0.°48	1.°16 ± 0.°63	15 ± 2	1.°58 ± 0.°45	1.°23 ± 0.°58	24 ± 4

Notes. For the spectral line (RRL, CO and H I), gamma-ray, and pulsar data the amplitudes are in units of K km s^{-1}, cm^{-2} s^{-1} sr^{-1} and number counts respectively. The pulsar data are at $N_{side} = 32$.

6. Discussion of the components

In Sect. 5.2 (Fig. 5) we showed the longitude distribution of the emission at $b = 0°$ from $l = 270° \rightarrow 0° \rightarrow 90°$ in different frequency bands from radio to FIR. The strongest emission is clearly associated with the inner spiral arms in quadrants IV ($l = 270°–360°$) and I ($l = 0°–90°$). First, we consider each

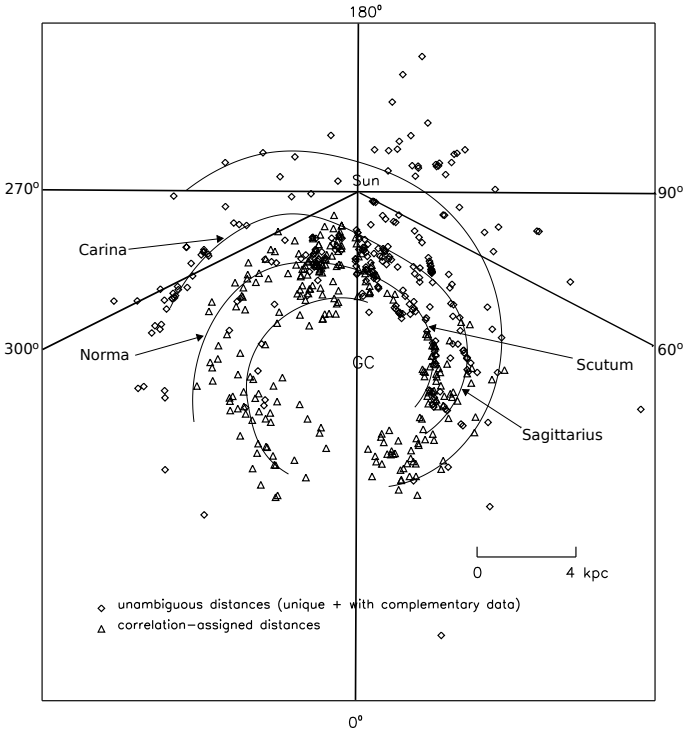

Fig. 3. Distribution of star-forming regions (H II regions) in the inner Galaxy, from Paladini et al. (2004, Fig. 12), with the $l = 300° \rightarrow 0° \rightarrow 60°$ sector indicated. The relevant spiral arms are also indicated.

emission component in turn, taking account of the latitude distribution and its expected spectral index to be used in the subsequent component separation. Then we determine SEDs at intervals along the Galactic plane at $b = 0°$, and the longitude distribution of each emission component between $l = 300°$ and 60°.

6.1. The free-free component

RRLs provide a direct estimate of the free-free emission on the Galactic plane that is unaffected by the absorption that has to be taken into account for the Hα measures that are commonly used at intermediate latitudes. We have a fully sampled map of the RRL emission for the region $l = 20°$ to 44° and $b = -4°$ to +4° (Alves et al. 2012), which can be used as a robust measure of the free-free emission in this range (Dickinson et al. 2003). These RRL data can be used to check the calibration of the FastMEM free-free estimate for the rest of the plane considered in this study (the parameters used are outlined in Sect. 4 and Appendix A). The ratio of the FastMEM brightness amplitude to the WMAP MEM value for the narrow component is 1.02 ± 0.05, while a similar comparison between the FastMEM and the RRL brightness temperatures gave a ratio of 1.19 ± 0.06. The question of systematic errors in the different datasets or analyses is discussed in Appendix A.

A possible systematic error in RRL free-free estimates is the uncertainty in electron temperature. We have adopted an average value of 6000 K (Alves et al. 2012); an increase of this value by 600 K would increase the brightness temperature by 10%. No correction has been applied for non-LTE factors (Stark broadening and stimulated emission), which act in opposite senses and which in any case are small at 1.4 GHz in low-density regions such as the diffuse gas on the Galactic plane (Shaver 1980; Gordon & Sorochenko 1990). We assign an overall error of 15% in the amplitude of the free-free contribution.

In addition, there are possible systematic errors in the FastMEM analysis, such as the contribution from the other emission components in the frequency range used in the analysis. Tests by varying the input parameters by reasonable amounts indicated that systematic effects were less than 10% (see Appendix A). On the basis of these results we adopt a conversion factor of 1.10 for the RRL data and use the FastMEM data reduced by 10% where the RRL data are not available.

The latitude distribution of the $l = 20°$ to 30° region of the narrow free-free component determined from RRLs at 1.4 GHz and from FastMEM is compared with the WMAP 60.7 GHz and the *Planck* 70.4 GHz total emission in Fig. 6, where the amplitudes have been normalized at $b = 0°$; only the narrow components are plotted. The 60.7 and 70.4 GHz emission is mainly free-free (70–90%) as will be shown in Fig. 9 (see Sect. 6.4). The 60.7 and 70.4 GHz latitude profiles from the two space missions are essentially identical.

Table 3 gives the intrinsic width of each of the free-free related components for the four longitude ranges under study. The average intrinsic width of free-free calculated from the RRL analysis for $l = 20°$–40° is 0.°92 ± 0.°05. The width of the emission at velocities corresponding to the Sagittarius and the Scutum arms is somewhat narrower at 0.°85 ± 0.°03 and 0.°78 ± 0.°01 respectively (Alves et al. 2012). The average of the 60.7 and 70.4 GHz FWHM is 1.°18 ± 0.°03. The FWHM value found from FastMEM is 1.°07 ± 0.°05. We conclude that the FWHM of the free-free emission is 1.°06 ± 0.°05 in the longitude range $l = 20°$–40° using all the free-free data. A similar result is found for the $l = 330°$–340° range; the $l = 320°$–330° range is broader in all components by a factor of 1.35 ± 0.05 due to bright structures adjacent to the plane.

The related data from the literature include the 99 GHz line of CS $J = 2 \rightarrow 1$, which identifies the regions of dense gas that are the sites of massive OB star formation (Bronfman et al. 2000). This line is integrated through the Galaxy and as published is averaged over the full longitude range; 79% lies in quadrants IV and I of the inner Galaxy. The CS FWHM is 0.°90 ± 0.°05, which Bronfman et al. estimate as 74 pc within the solar circle at distances of $R_G = 0.5$–$0.8\,R_\odot$ from the Galactic centre. Wood & Churchwell (1989) have identified the regions of massive star formation in molecular clouds, including ultracompact H II regions, by using their FIR two-colour properties. They find that the distribution of massive star candidates has a FWHM of 0.°83 ± 0.°05 corresponding to a scale height 0.°6 ($e^{-|b|/b_0}$ with $b_0 = 0.°6$); this is equivalent to a FWHM of 125 pc at an average distance of 8.5 kpc. We see that the OB-star latitude widths of 0.°83 are significantly narrower than those of the free-free emission as determined by the RRLs and the component separation results. This implies that the ionizing radiation from the OB stars is not fully absorbed in the dense molecular clouds in which they are born, but escapes into the surrounding lower density gas that it ionizes. Some of the broadening of the 60.7 and 70.4 GHz channels relative to the RRL emission is due to the contribution from AME, which will have the same width as the broader 100 μm dust listed in Table 2. AME in the 60–70 GHz range is 10–20% of the free-free as given by the SEDs.

The free-free width from RRLs (0.°92 ± 0.°05) is significantly less than that of the total gas density as measured by the CO (1.°13 ± 0.°06), 100 μm dust (1.°24 ± 0.°09), and *Planck* 545 GHz

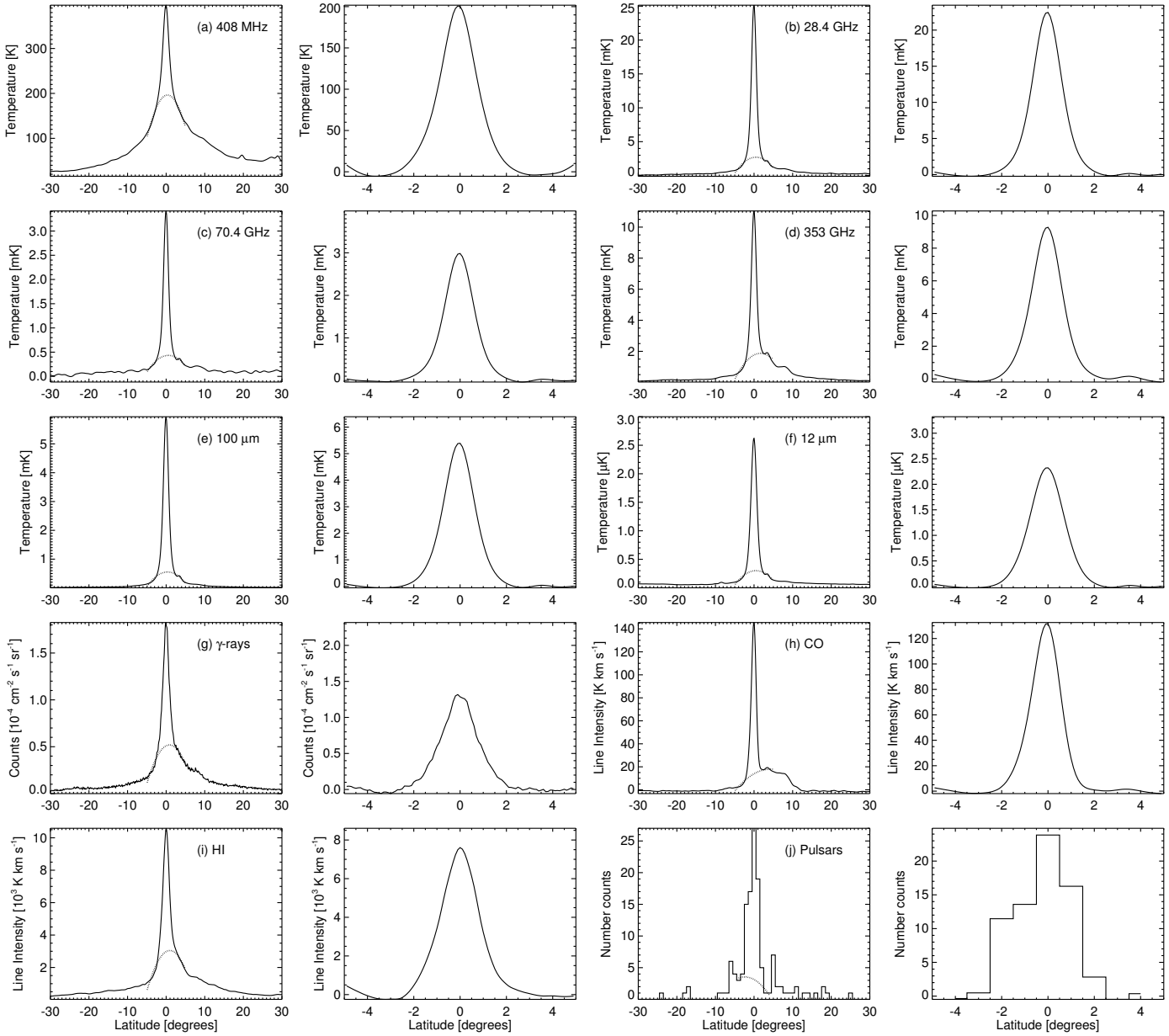

Fig. 4. Latitude distribution of various components averaged over the longitude range 20° to 30°. The first and third columns show the total emission (solid line) with the parabolic fit (dotted line) and the second and fourth columns show the narrow component. The pulsar data are at $N_{\rm side} = 64$ to account for the low sampling and include all ages; young and old pulsars are shown separately in Fig. 7. The northern Gould Belt system can be seen at positive latitudes at all frequencies. The broad 15° wide synchrotron component is evident in the 408 MHz cut.

(1°.33 ± 0°.08). This indicates that the fractional ionization decreases away from the OB stars on the plane.

We can compare the latitude distribution of the free-free emission, which is proportional to the emission measure (EM = $\int n_{\rm e}^2 {\rm d}l$), with the dispersion measure (DM = $\int n_{\rm e} {\rm d}l$) obtained from pulsar measurements. Narrow and broad $n_{\rm e}$ distributions have been identified in modelling the Galactic electron distribution (Cordes & Lazio 2002, 2003; Lorimer et al. 2006; Berkhuijsen et al. 2006; Gaensler et al. 2008). These studies give a thin component with thickness FWHM of 190 pc and a thick disk estimated to be in the range 900−1800 pc. They are mainly based on nearer pulsars as compared whilst the free-free emission is integrated through the depth of the Galaxy. We would expect the free-free to have a narrower distribution because of its dependence on $n_{\rm e}^2$ (Gaensler et al. 2008). This is indicated by the present data for the inner Galaxy where the FWHM of the free-free emission in the Sagittarius and Scutum arms has a FWHM of 100 pc (Alves et al. 2012). A level of clumping (filling factor) is required to bring the EM and DM into agreement. This clumping is already evident in the EM data (Reynolds et al. 1998; Berkhuijsen & Müller 2008; Alves et al. 2012).

6.2. Synchrotron

6.2.1. Separation of free-free and synchrotron

There is a long-standing difficulty of separating free-free and synchrotron emission on the Galactic plane (e.g., Broadbent et al. 1989; Bennett et al. 2003; Paladini et al. 2003; Sun et al. 2011). This problem can be solved by using RRL data. Three

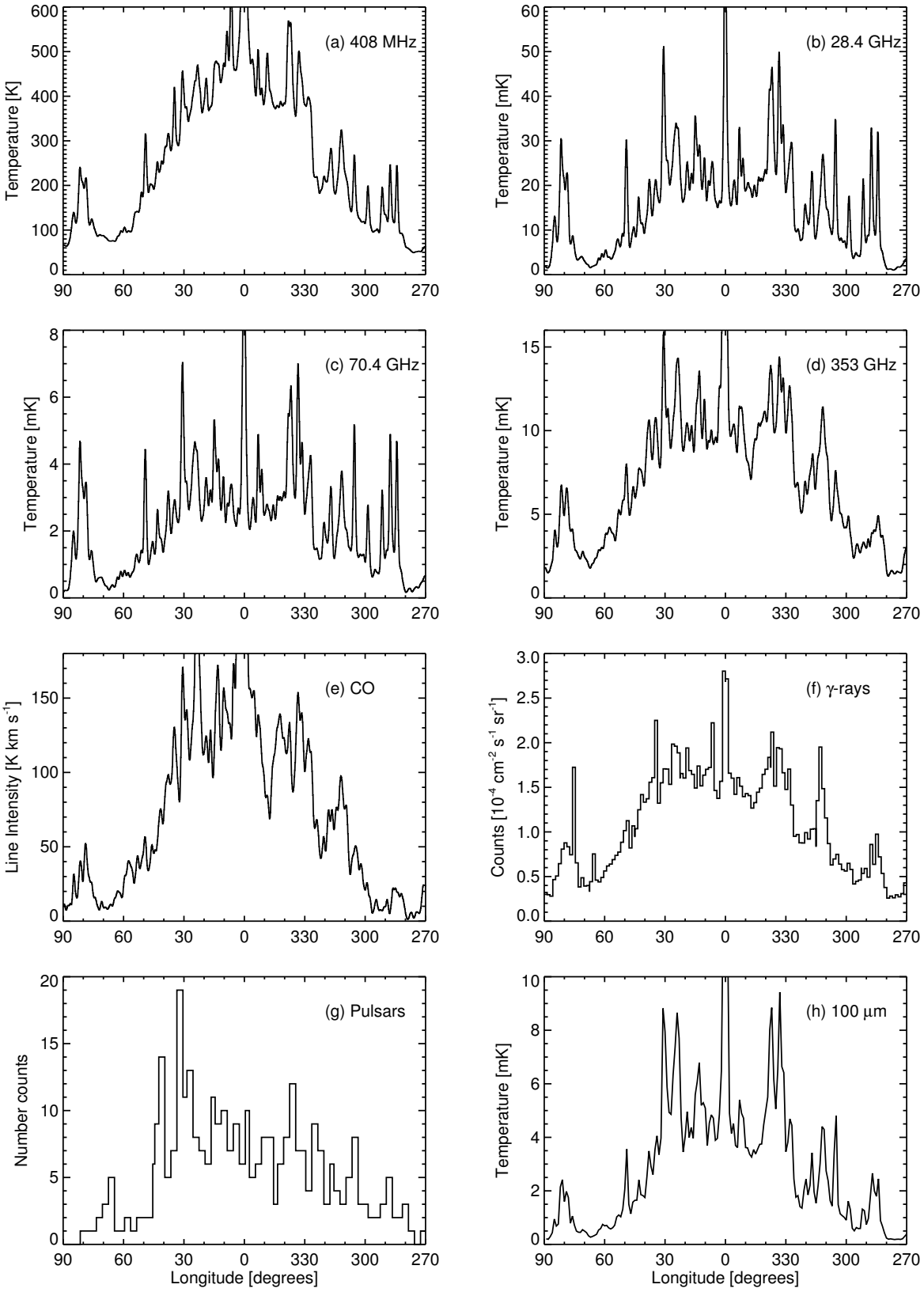

Fig. 5. Longitude distribution of emission components along the Galactic plane at $b = 0°$ in the range $l = 90°$ to $270°$. The data are all smoothed to 1° resolution except the gamma-ray data with a FWHM of 88′. The components shown are 408 MHz (mainly synchrotron), 28.4 GHz (similar AME and free-free), 70.4 GHz (mainly free-free), 353 GHz (dust), CO, gamma-rays, pulsar numbers (representing supernovae), and 100 μm. The gamma-ray and pulsar data are at $N_{\rm side} = 64$ and $N_{\rm side} = 32$ respectively, to account for the relatively low sampling. The pulsar data are uniformly surveyed from $l = 270°$ to 40°; at $l = 40°$ to 90° the survey sensitivity is lower. The Galactic centre is off-scale so that the diffuse emission can be displayed.

Table 3. Intrinsic latitude FWHM of free-free emission and related distributions for four longitude ranges.

Data	Intrinsic width [degrees]				Source of data
	l = 20°–30°	l = 30°–40°	l = 320°–330°	l = 330°–340°	
RRL	0.°90 ± 0.°06	0.°93 ± 0.°10	...	...	Alves et al. (2012)
60.7 GHz	1.°15 ± 0.°03	1.°21 ± 0.°09	1.°64 ± 0.°03	1.°18 ± 0.°06	WMAP
70.4 GHz	1.°15 ± 0.°03	1.°23 ± 0.°11	1.°67 ± 0.°05	1.°19 ± 0.°07	*Planck*
`FastMEM` estimate	1.°05 ± 0.°07	1.°06 ± 0.°07	1.°49 ± 0.°01	1.°10 ± 0.°12	This paper
OB stars (CS dense clouds)	0.°90 ± 0.°05	0.°90 ± 0.°05	0.°90 ± 0.°05	0.°90 ± 0.°05	Bronfman et al. (2000)[a]
OB stars (molecular clouds)	0.°83 ± 0.°05	0.°83 ± 0.°05	0.°83 ± 0.°05	0.°83 ± 0.°05	Wood & Churchwell (1989)[a]
100 μm	1.°23 ± 0.°11	1.°25 ± 0.°13	1.°66 ± 0.°04	1.°23 ± 0.°02	IRAS
CO	1.°09 ± 0.°12	1.°17 ± 0.°05	1.°70 ± 0.°03	1.°26 ± 0.°01	Planck Collaboration XIII (2014)
545 GHz	1.°22 ± 0.°10	1.°40 ± 0.°14	1.°76 ± 0.°03	1.°30 ± 0.°17	*Planck*

Notes. [(a)] Longitude range l = 270°–90°.

Table 4. Intrinsic latitude FWHM of synchrotron and related data for four longitude ranges.

Data	Intrinsic width [degrees]				Source of data
	l = 20°–30°	l = 30°–40°	l = 320°–330°	l = 330°–340°	
408 MHz	1.°63 ± 0.°14	1.°63 ± 0.°16	2.°14 ± 0.°08	1.°70 ± 0.°09	Haslam et al. (1982)
1.4 GHz	1.°60 ± 0.°11	1.°61 ± 0.°13	2.°02 ± 0.°07	1.°57 ± 0.°19	Reich (1982)
2.3 GHz	1.°47 ± 0.°10	1.°45 ± 0.°09	1.°97 ± 0.°12	1.°50 ± 0.°12	HartRAO courtesy of J. Jonas
23 GHz polarization	1.°66 ± 0.°08	1.°18 ± 0.°15	2.°94 ± 0.°32	1.°84 ± 0.°22	WMAP Lambda
545 GHz	1.°22 ± 0.°10	1.°40 ± 0.°14	1.°76 ± 0.°03	1.°30 ± 0.°17	*Planck*
100 μm	1.°23 ± 0.°11	1.°25 ± 0.°13	1.°66 ± 0.°04	1.°23 ± 0.°02	IRAS
CO	1.°09 ± 0.°12	1.°17 ± 0.°05	1.°70 ± 0.°03	1.°26 ± 0.°01	Planck Collaboration XIII (2014)
Gamma-rays	1.°18 ± 0.°11	1.°37 ± 0.°15	1.°75 ± 0.°11	1.°22 ± 0.°17	*Fermi*
Pulsars[a]	1.°15 ± 0.°63	1.°23 ± 0.°58	1.°16 ± 0.°63	1.°23 ± 0.°58	ATNF Pulsar Catalogue

Notes. [(a)] Age < 10^6 yr .

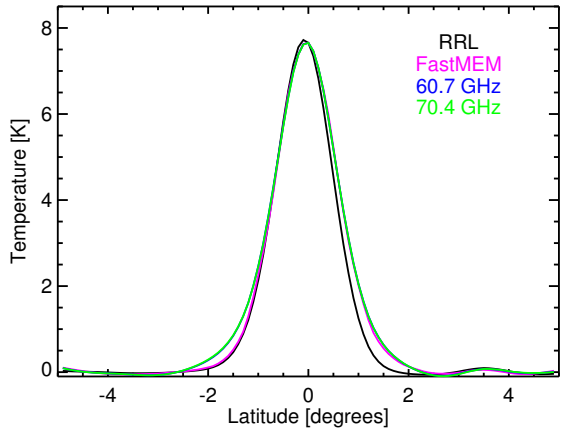

Fig. 6. Latitude cuts for the narrow free-free-related component in the longitude range l = 20° to 30° for RRLs, `FastMEM`, WMAP 60.7 GHz, and *Planck* 70.4 GHz. These are normalized to match the `FastMEM` solution at b = 0° in order to show their relative widths. The re-scaled 60.7 GHz and 70.4 GHz cuts match at all latitudes and are thus not visible separately.

well-calibrated maps of synchrotron continuum emission with angular resolution better than 1.°0 are available, namely those at 0.408, 1.4, and 2.3 GHz. For the longitude range l = 20°–44° these maps can be corrected for free-free emission using RRL data (Alves et al. 2012). Over this longitude range at b = 0°, the mean brightness temperature of the synchrotron narrow emission (5.0 K) is similar to that of the free-free emission (4.6 K) at 1.4 GHz. Accordingly, the free-free emission in the narrow component is 0.31 and 1.43 times the synchrotron at 0.408 and 2.3 GHz respectively, assuming a synchrotron spectral index of −3.0. For a spectral index of −2.7 these ratios are 0.44 and 1.22.

Figure 7 shows the raw latitude cuts for the three frequencies, 0.408, 1.4, and 2.3 GHz, that contain significant amounts of synchrotron emission, along with cuts for related emission mechanisms. The ratio of the brightness of the broad synchrotron disk to that of the narrow disk is 0.75, 0.57, and 0.43 at 0.408, 1.4, and 2.3 GHz respectively, for the longitude range l = 20°–30°. After correcting for the contribution from free-free, these ratios are similar (1.18, 1.12, 0.98), suggesting that the spectral indices of the narrow and the broad disk synchrotron components are similar in the range 408 MHz to 2.3 GHz. We might expect the latitude distribution of the synchrotron emission at ∼1 GHz and *Planck* LFI frequencies to be similar since the diffusion length in ∼10 μG magnetic fields is greater than 1 kpc for the 4−50 GeV electrons responsible (Mertsch & Sarkar 2010, 2013). We see that the polarized 23 GHz width of the inner Galaxy is indeed similar to the ∼1 GHz widths (Fig. 7 and Table 4). This same is not true of the larger-scale haze emission (Mertsch & Sarkar 2010; Dobler 2012; Planck Collaboration Int. IX 2013).

We note that at $|b| > 5°$ the free-free emission is <5% of the value at b = 0° and accordingly we conclude that the broad synchrotron component at $|b|$ = 5° is essentially uncontaminated

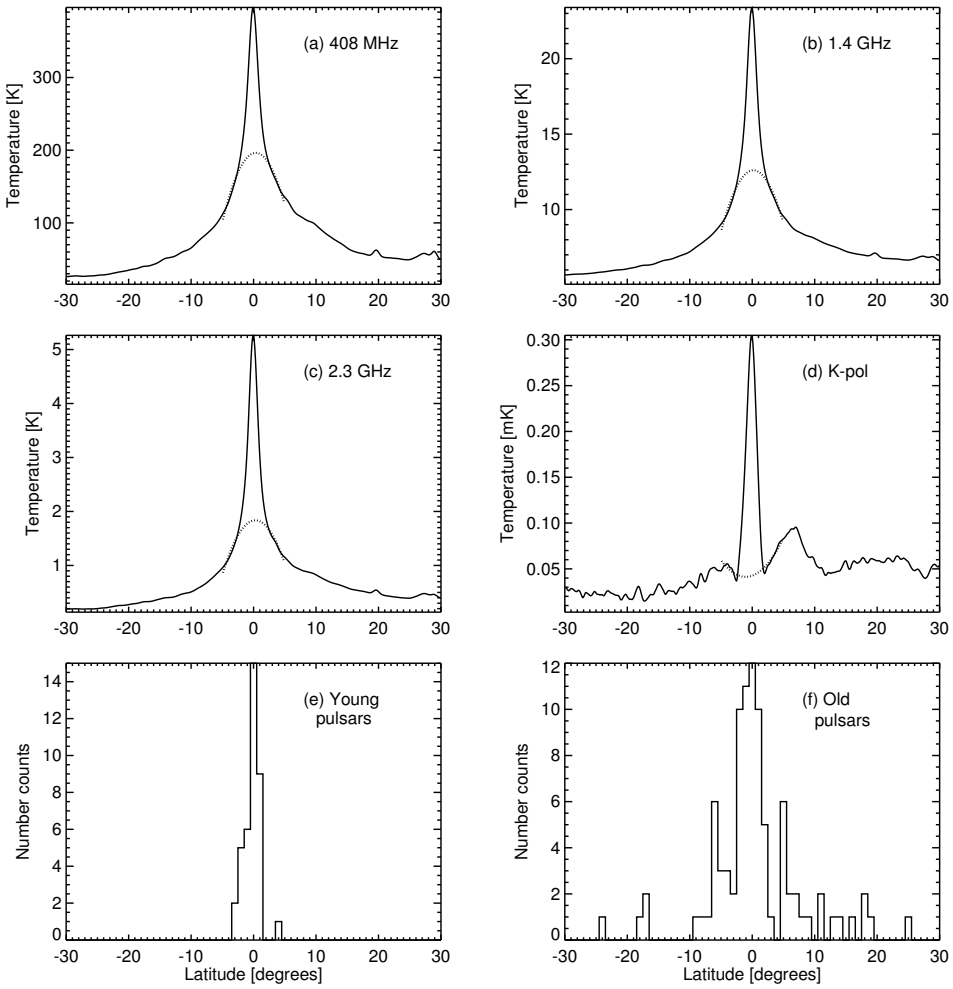

Fig. 7. Latitude cuts in bands relevant to synchrotron emission averaged over the longitude range 20°–30°. These are 0.408, 1.4, and 2.3 GHz, WMAP *K*-band polarized intensity, and pulsar number counts. A reference age of 10^6 yr is chosen to define young and old pulsars. No parabolic fit is made to the separate pulsar population cuts.

by free-free (at levels of 1.9, 3.4, 5.2% at 0.408, 1.4. and 2.3 GHz respectively).

Table 4 gives the intrinsic widths of the narrow, synchrotron-dominated, low-frequency latitude distribution for the longitude ranges l = 20°–30°, 30°–40°, 320°–330°, and 330°–340°. Note that in going from 0.408 to 2.3 GHz the free-free content becomes comparable with the synchrotron emission. This may explain the slight narrowing at 2.3 GHz. Typical synchrotron FWHM intrinsic widths are 1.°7. This value may be compared with the width of the polarized emission in the WMAP 23 GHz *K*-band data (Bennett et al. 2013), which is 1.°73 ± 0.°13; the polarized emission is the only direct measure of a synchrotron component that is uncontaminated by free-free at WMAP and *Planck* frequencies. Both these values are significantly greater than the total matter-width as represented by the dust as given by the *Planck* 545 GHz channel (1.°22) or the gas as given by the CO (1.°10) and the CS (0.°83) distributions.

6.2.2. Origin of the narrow component

We turn now to a comparison of the widths of the distributions of the synchrotron emission, pulsars, and gamma-rays, which all originate in the supernovae associated with the collapse of massive OB stars with FWHMs of 1.°2–1.°3.

(a) Pulsars. Pulsars are formed during the core collapse of the OB stars with ejection velocities having a component perpendicular to the Galactic plane of 100−200 km s^{-1} (Chatterjee et al. 2009). Figure 7 shows the broader distribution of pulsars older than 10^6 yr relative to that of the younger pulsars in the longitude range l = 20°–30°. The width for younger pulsars is ∼2°, which is comparable to the width of the synchrotron emission and significantly broader than that of the nascent OB stars.

(b) Gamma-rays. Interstellar gamma-rays are produced by π_0-decay following the collision of relativistic cosmic ray protons with gas (principally atomic and molecular hydrogen). The relativistic cosmic ray protons and electrons themselves are accelerated by diffusive shock acceleration at collisionless shocks driven by the SN explosions (Blandford & Ostriker 1978). The 1−100 GeV CREs produce radio synchrotron emission in the enhanced magnetic fields of the SNRs while the low energy ($\lesssim$1 GeV) electrons can produce gamma-ray bremsstrahlung. The CR protons generate gamma-rays by π_0-decay in the swept-up SN gas or in any adjacent gas. IC gamma-rays may also be produced in regions of high radiation field. Good examples of young SNRs demonstrating these emission processes include Cas A, the Crab nebula, and W49B

(Abdo et al. 2010a,b,d). Accordingly it is expected that the distributions of CR electrons and protons and gamma-rays will follow that of the pulsars (Strong et al. 2010). The relativistic electrons responsible for the Galactic synchrotron emission are initially held in the magnetic field of the expanding SN shell and will escape into the ISM as its magnetic field weakens (Strong et al. 2011; Mertsch & Sarkar 2013). The escaping CR protons generated in the continuing star-formation and subsequent collapse on the Galactic plane are expected to interact with the atomic and molecular hydrogen on the Galactic disk to produce a gamma-ray distribution similar to that of the gas. Table 4 indicates that the gamma-ray FWHM (∼1.°3) is indeed consistent with the higher *Planck* frequencies, 100 μm, and CO with a FWHM of 1.°2–1.°3.

We now consider the possible reasons for the greater width of the synchrotron emission distribution as compared with that of the nascent OB stars. After the birth of an SNR the high energy CREs will escape, leaving the low-energy (2−100 GeV) CREs trapped by magnetic fields in the SNR emitting with a brightness temperature spectral index of $\beta_{\rm synch} \approx -2.5$; this is a mean value at 1 GHz although there is a spread of ±0.2 (Green 2009; Delahaye et al. 2010). Those CREs that escape will have radiative energy losses and steepen to $\beta_{\rm synch} \approx -3.0$ at tens of gigahertz in the *Planck* frequency range. These eventually escape into the Galactic halo at intermediate latitudes with a thickness estimated at 1 to 10 kpc (Strong 2011; Strong et al. 2011) and have this spectral index of −3.0 (Davies et al. 2006; Gold et al. 2011; Jaffe et al. 2011; Ghosh et al. 2012). Assuming no reacceleration, the spectral indices will also apply to the narrow Galactic plane synchrotron component (Strong et al. 2011). We propose that the narrow synchrotron layer is comprised of the SNRs of all ages up to the time the remnants merge into the general ISM at intermediate latitudes at a height of several kiloparsecs. On the timescale of the oldest SNRs (50 000 yr, Milne 1971) the diameters reach ∼30 pc. The observed synchrotron broadening (1.°7) corresponds to an effective FWHM of 170 pc at a mean distance of 6 kpc. This extra broadening relative to the OB stars (80 pc) is most likely made up of SNR expansion and proper motions of several tens of kilometres per second. Over an effective SNR lifetime of 10^5–10^6 yr, which is also the age of the pulsars, these motions could account for this broadening. On this timescale about 10^3–10^4 supernovae and (O-star) progenitors would have been born.

Strong confirmation of the identification of a narrow synchrotron component on the Galactic plane is provided by the WMAP observation of 23 GHz polarization with the same width as the narrow component of the 408 MHz synchrotron total intensity (Fig. 7 and Table 4). The magnetic field alignment is parallel to the Galactic plane and is the ordered field that permeates the Galactic disk. The fractional polarization on the Galactic plane at WMAP frequencies, where synchrotron emission is 10% of the total intensity at most, can be estimated using the 408 MHz data (corrected for free-free) and assuming a spectral index. If a spectral index of −3.0 between 408 MHz and WMAP frequencies is assumed, as indicated by various observations (Davies et al. 2006; Kogut et al. 2007; Miville-Deschênes et al. 2008; Dunkley et al. 2009b; Gold et al. 2009, 2011; Ghosh et al. 2012), the percentage polarization of the narrow synchrotron component is 50%. If the spectral index were −2.8, the polarization would be 30% in this 170 pc-wide component. In either case the percentages for the narrow Galactic plane component are evidently higher than at intermediate latitudes where it has been found to be 10−20% on average in an earlier analysis of WMAP data (Kogut et al. 2007; Macellari et al. 2011), however it can be up to 40−50% in some regions. This reflects the fact that the aligned fraction of the field is greater on the plane and is therefore more significant in the narrow latitude component we have identified.

The lower polarization (5−10% averaged over l = 20°–30° in Fig. 7) in the $|b|$ range 2°–5° is the consequence of the superposition of filaments leaving the Galactic plane having magnetic fields with a major component perpendicular to the plane, thereby cancelling the polarization parallel to the plane.

6.3. Thermal (vibrational) dust

Two types of dust grain contribute to FIR emission. Larger grains emit in the COBE-DIRBE/*Planck* bands and the IRAS 60 and 100 μm bands. Smaller warm grains radiate in the 25 and 12 μm IRAS bands and are also responsible for the AME emission at gigahertz frequencies. In this section we examine the latitude distribution and spectrum of the large grains.

6.3.1. Thermal dust – latitude distribution

Figure 8 shows latitude cuts at three *Planck* bands that sample vibrational dust, along with relevant ancillary data. The narrow inner Galaxy dust distribution is clear and is the major component on the plane in these bands. The weaker extended emission at positive latitudes is from the northern Gould Belt, which lies within the local spiral arm. The intrinsic latitude widths of the emission in the *Planck* bands for the four longitude ranges 20°–30°, 30°–40°, 320°–330°, 330°–340° are given in Table 5 along with widths for ancillary data of interest. The widths at the four *Planck* frequencies in the range 143−857 GHz are remarkably consistent at 1.°23 ± 0.°02, 1.°40 ± 0.°03, and 1.°30 ± 0.°02 for l = 20°–30°, 30°–40°, and 330°–340° respectively; at l = 320°–330° the widths are greater by a factor of 1.35 ± 0.05. This agreement shows that these frequency bands are all sampling dust with the same emission properties. The widths of the FIR bands of COBE-DIRBE (140 μm, 240 μm) and the 100 μm band of IRAS are consistent within each of the three longitude ranges with FWHM widths of 1.°22 ± 0.°02, 1.°27 ± 0.°03, and 1.°25 ± 0.°02, similar to those of the *Planck* bands. In each of the longitude ranges, on going to shorter wavelengths the width falls to a minimum of 1.°13 ± 0.°02 at 60 μm and rises again to 1.°44 ± 0.°02 at 12 μm; this is the small grain dust thought to be responsible for AME. We consider the implication of these results further in Sect. 7.

We might expect the dust distribution at *Planck* frequencies to follow that of the gas, as indicated by the strong correlation between the *Planck* sky at HFI frequencies and H I (Planck Collaboration XIX 2011). We should therefore compare the direct dust data with other estimates of the total gas mass distribution in the Galactic plane. CO is generally considered to be a proxy for molecular hydrogen in the denser phases. The CS molecule has also been proposed as an indicator of the denser molecular clouds in which star-formation is currently occurring (Bronfman et al. 2000). CO is an indicator of somewhat less dense gas. The intrinsic width of CS averaged over the inner Galaxy is 0.°83 while that of the CO in the longitude ranges 20°–30° and 30°–40° is 1.°09 and 1.°17 respectively, showing that denser star-forming gas has a narrower distribution than that of the dust measured in the *Planck* HFI channels.

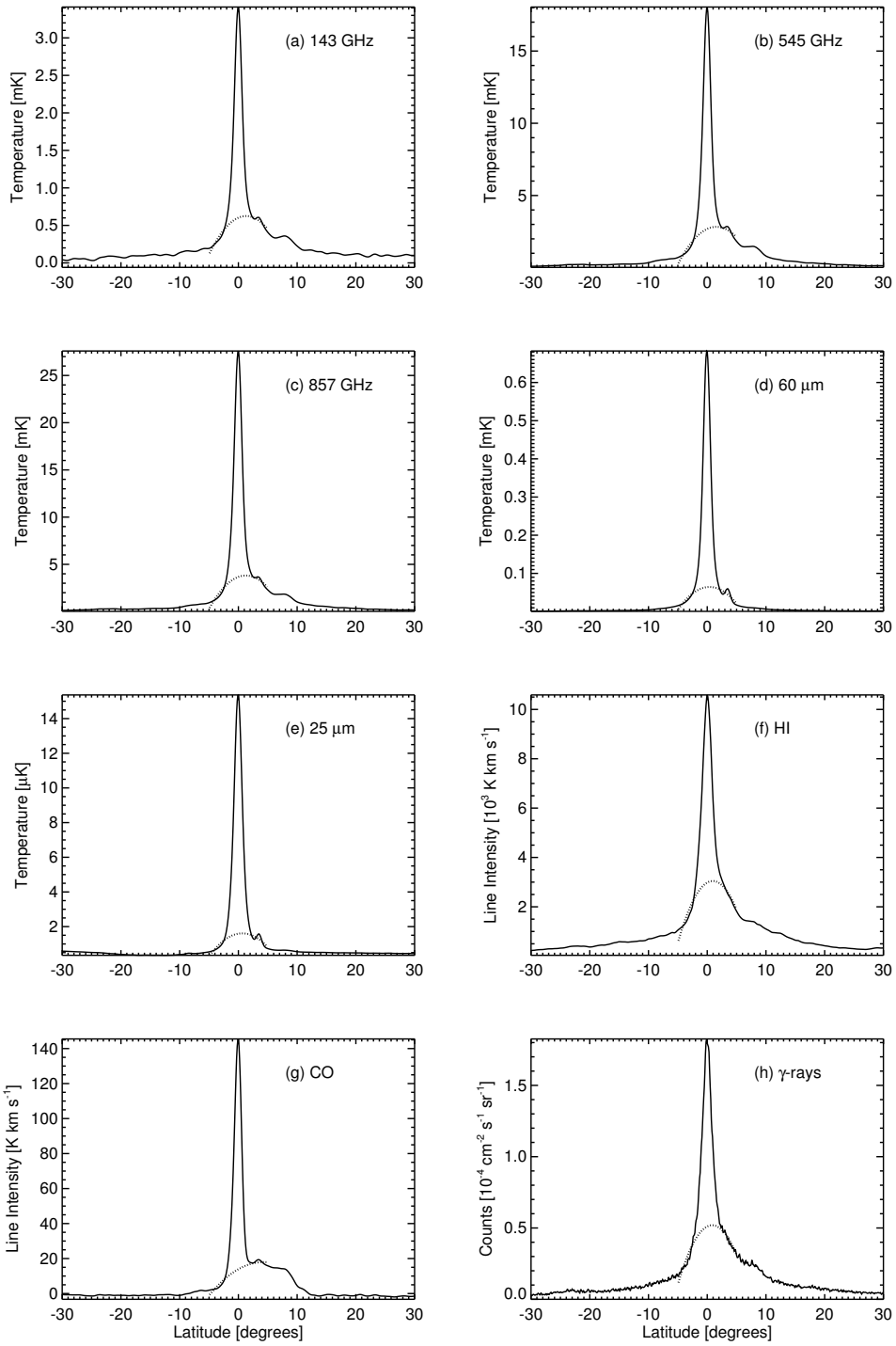

Fig. 8. Latitude profiles of *Planck* frequency bands and ancillary data relating principally to thermal dust, for $l = 20°–30°$.

Another indicator of the total gas surface density is the gamma-ray brightness (Grenier et al. 2005). The gamma-ray intrinsic width averaged over the three longitude ranges ($l = 20°–30°$, $30°–40°$, and $330°–340°$) is $1\overset{\circ}{.}26 \pm 0\overset{\circ}{.}05$, similar to the molecular indicators. In contrast, the apparent H I width is significantly greater at $1\overset{\circ}{.}98 \pm 0\overset{\circ}{.}05$ (Tables 5 and 9). The conversion of the observed latitude profile to a true H I surface density profile requires a correction for the higher optical depth on the Galactic plane, leading to a narrower FWHM. The total gas distribution (H I + H_2) will be narrower again, approaching the gamma-ray FWHM.

6.3.2. Thermal dust spectrum via SEDs

The wide frequency coverage of the present data set allows a well-sampled spectral energy distribution (SED) to be determined at points along the Galactic plane. The four emission components (synchrotron, free-free, AME, and thermal dust) all

Table 5. Intrinsic latitude FWHM of thermal dust emission and related data for four longitude ranges.

Data	Intrinsic width [degrees]				Source of data
	$l = 20°$–$30°$	$l = 30°$–$40°$	$l = 320°$–$330°$	$l = 330°$–$340°$	
143 GHz	$1.^\circ24 \pm 0.^\circ12$	$1.^\circ43 \pm 0.^\circ18$	$1.^\circ79 \pm 0.^\circ17$	$1.^\circ31 \pm 0.^\circ06$	*Planck*
353 GHz	$1.^\circ22 \pm 0.^\circ10$	$1.^\circ41 \pm 0.^\circ16$	$1.^\circ77 \pm 0.^\circ04$	$1.^\circ30 \pm 0.^\circ06$	*Planck*
545 GHz	$1.^\circ22 \pm 0.^\circ10$	$1.^\circ40 \pm 0.^\circ14$	$1.^\circ76 \pm 0.^\circ03$	$1.^\circ30 \pm 0.^\circ17$	*Planck*
857 GHz	$1.^\circ23 \pm 0.^\circ11$	$1.^\circ36 \pm 0.^\circ11$	$1.^\circ75 \pm 0.^\circ02$	$1.^\circ29 \pm 0.^\circ17$	*Planck*
1249 GHz	$1.^\circ21 \pm 0.^\circ09$	$1.^\circ30 \pm 0.^\circ05$	$1.^\circ71 \pm 0.^\circ02$	$1.^\circ26 \pm 0.^\circ13$	COBE-DIRBE
2141 GHz	$1.^\circ23 \pm 0.^\circ11$	$1.^\circ28 \pm 0.^\circ03$	$1.^\circ69 \pm 0.^\circ07$	$1.^\circ26 \pm 0.^\circ01$	COBE-DIRBE
100 μm	$1.^\circ23 \pm 0.^\circ11$	$1.^\circ23 \pm 0.^\circ13$	$1.^\circ66 \pm 0.^\circ04$	$1.^\circ23 \pm 0.^\circ02$	IRAS
60 μm	$1.^\circ11 \pm 0.^\circ01$	$1.^\circ13 \pm 0.^\circ02$	$1.^\circ53 \pm 0.^\circ03$	$1.^\circ14 \pm 0.^\circ02$	IRAS
25 μm	$1.^\circ32 \pm 0.^\circ05$	$1.^\circ37 \pm 0.^\circ12$	$1.^\circ70 \pm 0.^\circ04$	$1.^\circ26 \pm 0.^\circ01$	IRAS
12 μm	$1.^\circ44 \pm 0.^\circ06$	$1.^\circ44 \pm 0.^\circ06$	$1.^\circ83 \pm 0.^\circ09$	$1.^\circ45 \pm 0.^\circ05$	IRAS
Gamma-rays	$1.^\circ18 \pm 0.^\circ11$	$1.^\circ37 \pm 0.^\circ15$	$1.^\circ75 \pm 0.^\circ11$	$1.^\circ22 \pm 0.^\circ17$	*Fermi*
CO	$1.^\circ09 \pm 0.^\circ12$	$1.^\circ17 \pm 0.^\circ05$	$1.^\circ70 \pm 0.^\circ03$	$1.^\circ26 \pm 0.^\circ01$	Planck Collaboration XIII (2014)
CS	$0.^\circ90 \pm 0.^\circ05$	$0.^\circ90 \pm 0.^\circ05$	$0.^\circ90 \pm 0.^\circ05$	$0.^\circ90 \pm 0.^\circ05$	Bronfman et al. (2000)
H I	$1.^\circ86 \pm 0.^\circ12$	$2.^\circ03 \pm 0.^\circ09$	$2.^\circ19 \pm 0.^\circ09$	$2.^\circ06 \pm 0.^\circ10$	Hartmann & Burton (1997), Dickey & Lockman (1990)

Table 6. Thermal dust properties from SEDs using MILCA for CO and fitting two $\beta_{\rm dust}$ values.

Data	$l = 20°$–$30°$	$l = 30°$–$40°$	$l = 320°$–$330°$	$l = 330°$–$340°$	Average
$T_{\rm dust}$ (K)	20.79 ± 1.32	20.26 ± 1.25	19.11 ± 1.10	21.32 ± 1.40	20.37 ± 0.40
$\tau_{353} \times 10^4$	6.20 ± 0.55	5.51 ± 0.48	5.02 ± 0.41	6.35 ± 0.58	5.77 ± 0.22
$\beta_{\rm FIR}{}^a$	1.97 ± 0.14	1.92 ± 0.14	1.96 ± 0.14	1.92 ± 0.14	1.94 ± 0.03
$\beta_{\rm mm}{}^b$	1.71 ± 0.04	1.65 ± 0.04	1.64 ± 0.04	1.69 ± 0.05	1.67 ± 0.02
Reduced χ^2	0.33	0.30	0.51	0.51	0.41

Notes. [(a)] $\beta_{\rm FIR}$ is estimated for $\nu \geq 353$ GHz. [(b)] $\beta_{\rm mm}$ is estimated for $\nu < 353$ GHz.

have established spectral shapes, so the observed brightness temperature $T_{\rm b}$ can be expressed as a sum:

$$T_{\rm b} = T_{\rm synch}(\nu) + T_{\rm ff}(\nu) + T_{\rm d}(\nu) + T_{\rm AME}(\nu) + T_{\rm CMB}(\nu), \quad (1)$$

where

- $T_{\rm synch}$ has a brightness temperature spectral index $\beta_{\rm synch} = -2.7$ in the frequency range 0.408 to 2.3 GHz (Platania et al. 1998, 2003; Peel et al. 2012), which steepens to -3.0 at WMAP and *Planck* frequencies (Banday et al. 2003; Davies et al. 2006; Kogut et al. 2011; Ghosh et al. 2012).
- $T_{\rm ff}$ has a spectral index of -2.10 to -2.12 over the LFI frequency range and steepens -2.14 at 100 GHz due to the Gaunt factor (Draine 2011). The free-free brightness can be determined directly from RRLs, which can also be used to calibrate the `FastMEM` analysis.
- $T_{\rm d} = \tau_{\nu_0}(\nu/\nu_0)^{\beta_{\rm dust}} B(\nu, T_{\rm dust})$, where

$$B(\nu, T_{\rm dust}) = 2\,h\,\frac{\nu^3}{c^2}\,\frac{1}{{\rm e}^{h\nu/kT_{\rm dust}} - 1}\,, \quad (2)$$

  is a blackbody spectrum modified by a low frequency spectral index $\beta_{\rm dust}$, and τ_{ν_0} is the dust optical depth at a reference frequency $\nu_0 = 353$ GHz. There is strong evidence for a break in $\beta_{\rm dust}$, with a flatter value, $\beta_{\rm mm}$, at $\nu < 353$ GHz, and a steeper value, $\beta_{\rm FIR}$, at $\nu \geq 353$ GHz (Paradis et al. 2009; Gordon et al. 2010; Galliano et al. 2011; Planck Collaboration Int. XIV 2014).
- $T_{\rm AME}$ is calculated as a residual after correction for the other components but can also be fitted to models (Planck Collaboration XX 2011; Planck Collaboration Int. XII 2013).
- $T_{\rm CMB}$ is the CMB fluctuation amplitude on scales of 1° or larger appropriate to the present study. These signals are $<100\,\mu$K and can be neglected in comparison with the millikelvin Galactic plane signals.

The dust parameters $\beta_{\rm FIR}$, $\beta_{\rm mm}$, τ_{ν_0} and $T_{\rm dust}$ are determined from the fit to the *Planck* HFI data supplemented with the COBE-DIRBE data, where the spectral indices $\beta_{\rm FIR}$ and $\beta_{\rm mm}$ are fitted to the data above and below 353 GHz, respectively. The CO contribution at 100, 217 and 353 GHz is removed using the MILCA maps (Sect. 3.5). We perform a least-squares fit using the IDL `MPFIT` routine (Markwardt 2009), taking into account the noise (both statistical and systematic) and colour corrections to the HFI and DIRBE data.

Table 6 shows that the values for $T_{\rm dust}$, $\beta_{\rm FIR}$, and $\beta_{\rm mm}$ are similar in each of the four sections of the inner Galactic plane. The low values of reduced χ^2/d.o.f. with d.o.f. $= 5$ indicate that the errors assigned to the data are overestimates. The errors given for the average values in Table 6 are more realistic estimates of the scatter between the four regions. Our average values for the regions $l = 320°$–$340°$ and $l = 20°$–$40°$ using a FWHM of 1° on the Galactic plane are $T_{\rm dust} = 20.4 \pm 0.4$ K, $\beta_{\rm FIR} = 1.94 \pm 0.03$, and $\beta_{\rm mm} = 1.67 \pm 0.02$ (Table 6). These β values are in agreement with a similar analysis (Planck Collaboration Int. XIV 2014) of the region $l = 20°$–$44°$ at $|b| < 1°$, which found median values of $\beta_{\rm FIR} = 1.88$ and $\beta_{\rm mm} = 1.60$ with standard deviations of 0.08 and 0.06 respectively, which are the spread of values across the chosen region.

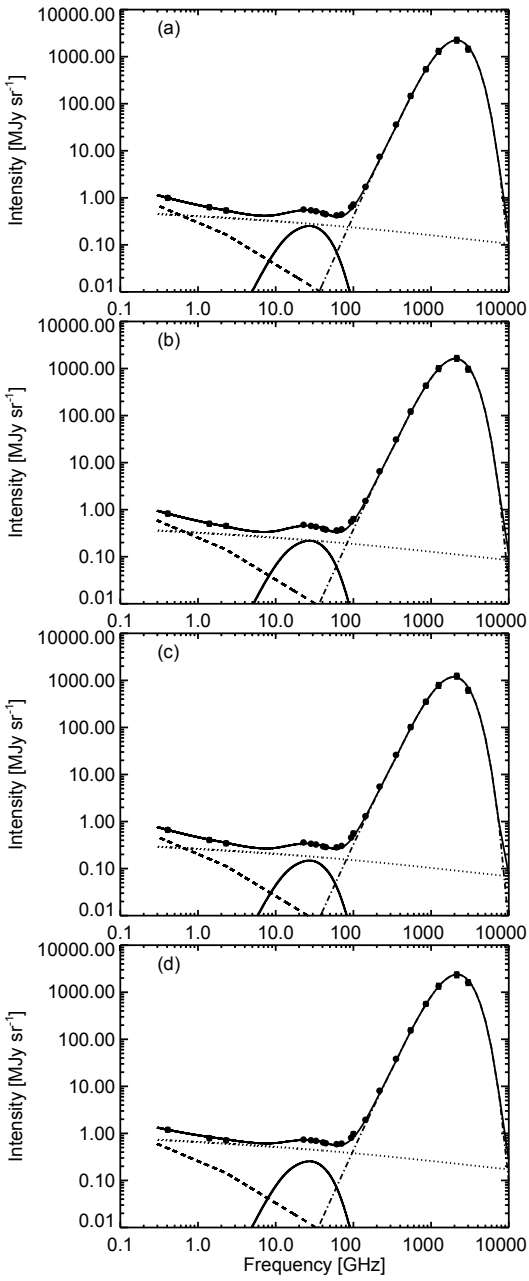

Fig. 9. SEDs over full frequency range 0.408 GHz to 3000 GHz, for the longitude ranges **a)** l = 20°–30°; **b)** 30°–40°; **c)** 320°–330°; and **d)** 330°–340°. The points show the total emission, which is separated into free-free from the RRL and FastMEM data (dotted line), synchrotron from the free-free-corrected 408 MHz data (dashed line) and thermal dust (dot-dashed line). The total of the four components is given by the full line. AME is the residual (long-dash-dotted line). The conversion factor from intensity to brightness temperature at 28.4 GHz is 40 mK MJy^{-1} sr.

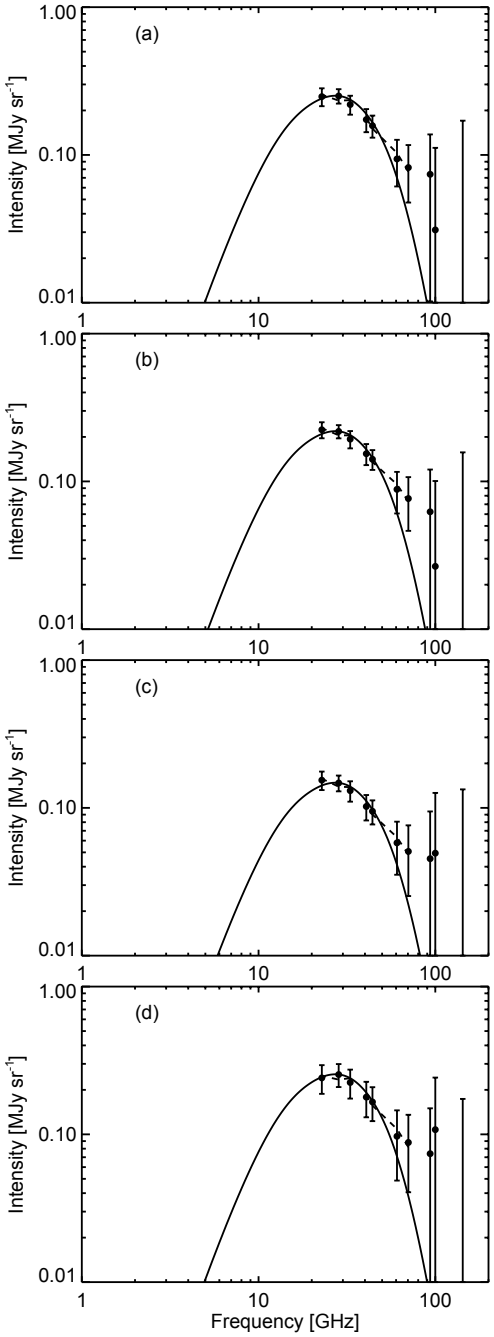

Fig. 10. AME spectra for the longitude ranges **a)** l = 20°–30°; **b)** 30°–40°; **c)** 320°–330°; and **d)** 330°–340°. The spectra cover the frequency range 23−143 GHz and are in units of intensity. The conversion factor from intensity to brightness temperature at 28.4 GHz is 40 mK MJy^{-1} sr.

Figure 9 shows the SEDs for Galactic plane emission averaged over the four 10° intervals l = 20°–30°, l = 30°–40°, l = 320°–330°, and l = 330°–340° at b = 0°. The synchrotron spectrum is a fit to the lower frequencies (0.408−2.3 GHz) with $\beta_{\rm synch}$ = −2.7 up to 2.3 GHz and $\beta_{\rm synch}$ = −3.0 at higher frequencies. The free-free emission is based on the RRL data supplemented by the FastMEM analysis using a spectral index of −2.10 to −2.12 over the LFI frequency range (Draine 2011). The two-component dust emission is derived from a least-squares fit to the HFI data as described above. The AME emission is the remainder and is shown as a fit to a equal combination of warm ionized medium (WIM) and molecular cloud (MC) models of AME emission (Ali-Haïmoud et al. 2009).

6.4. AME estimated from SEDs

Since AME is expected to be correlated with the dust distribution, on the plane it is not possible to use morphology to separate it from other emission components as is the case at higher latitudes. On the Galactic plane we use SEDs to separate the various emission components using their spectral shapes. Figure 9 shows the spectra of the synchrotron, free-free and thermal dust as described in Sect. 6.3.2. AME is the remainder of the total emission and is shown in more detail in Fig. 10 for the four

Table 7. AME fractions in the four longitude ranges shown in Figs. 9 and 10.

Parameter	l = 20°–30°	l = 30°–40°	l = 320°–330°	l = 330°–340°	Average
AME/total at 28.4 GHz	0.45 ± 0.05	0.48 ± 0.05	0.44 ± 0.05	0.36 ± 0.06	0.44 ± 0.03
Significance of the above	8.9σ	9.7σ	8.2σ	5.6σ	. . .
AME/free-free at 28.4 GHz	0.9 ± 0.1	1.0 ± 0.1	0.8 ± 0.1	0.6 ± 0.1	. . .
AME spectral index at 28.4 GHz	−2.2 ± 0.5	−2.3 ± 0.4	−2.3 ± 0.5	−2.1 ± 0.8	−2.2 ± 0.3
AME spectral index at 70 GHz	−3.4 ± 0.6	−3.3 ± 0.6	−3.3 ± 0.7	−3.3 ± 0.9	−3.3 ± 0.4

Notes. The spectral indices at 28.4 and 70 GHz are included.

Table 8. Comparison of AME with free-free and 100 μm emission in the innermost (l = 5°–30° and 330°–355°) and the outer (l = 30°–60° and 300°–330°) regions of the inner Galaxy as shown in Fig. 11.

Parameter	l = 5°–30° l = 330°–355°	l = 30°–60° l = 300°–330°	Average
AME/free-free at 28.4 GHz	0.71 ± 0.04	0.80 ± 0.04	0.75 ± 0.03
AME at 28.4 GHz/100 μm emission[a]	7.1 ± 0.4	9.8 ± 0.5	7.4 ± 0.3
AME at 28.4 GHz/total emission	0.42 ± 0.02	0.48 ± 0.01	0.45 ± 0.01

Notes. [(a)] The conversion factor at 28.4 GHz is 40 mK MJy^{-1} sr.

longitude ranges l = 20°–30°, 30°–40°, l = 320°–330° and 330°–340°. The combination of WIM and MC spinning dust models (Draine & Lazarian 1998b; Ali-Haïmoud et al. 2009) shown for comparison is a good fit to the data points. The peak emission is at ∼25 GHz, which is in agreement with the values of 25.5 ± 1.5 GHz for molecular clouds in the Gould Belt system at intermediate latitudes (Planck Collaboration Int. XII 2013). A study of AME regions (Planck Collaboration Int. XV 2014) found a peak frequency around 28 GHz.

The AME fractions of the 28.4 GHz total emission in the l = 20°–30°, 30°–40°, 320°–330°, and 330°–340° regions are given in Table 7. The errors shown in Fig. 10 and Table 7 are a combination of the uncertainties in the Gaussian fit of the amplitude of each latitude profile (and taking account of the error in the underlying broad component). These uncertainties are propagated in the models of free-free, synchrotron, and dust that are removed from the observations in order to derive the AME amplitude. The AME is well determined with significance in the range 5.6–9.7σ. The mean value of the AME-to-total fraction at 28.4 GHz is 0.44 ± 0.03.

As shown in Fig. 10 and Table 7 there is a significant steepening of the spectral index of the AME emission between 28.4 GHz ($\beta_{\rm AME}$ = −2.2 ± 0.3; obtained from 22.8, 28.4 and 33.0 GHz) and 70 GHz ($\beta_{\rm AME}$ = −3.3 ± 0.4; obtained from 40.7, 44.1, 60.7 and 70.4 GHz). The steepening is compatible with spinning dust models but is not well-defined due to the uncertainty in the extrapolation of the dust model below 100 GHz.

A question arises as to whether the 20–60 GHz excess is due to a population of ultracompact H II regions (Wood & Churchwell 1989; Kurtz 2002; Dickinson 2013). This matter is discussed in Planck Collaboration Int. XV (2014) where the 100 μm flux densities from IRAS are used to determine an upper limit to the contribution from ultracompact H II regions. We find that in the l = 20°–30° region ($|b| < 0.^\circ5$) there are 907 IRAS sources, of which 100 have colours that indicate them being candidate ultra compact H II regions. Summing their 100 μm flux densities, and converting to an upper limit at 15 GHz gives an average of 17 Jy deg^{-2}, or an upper limit of 2 mK at 28.4 GHz. This compares with the observed value of 23 mK in this region, as seen in Fig. 4. We conclude that ultracompact H II regions are a minor contribution to the emission on the Galactic plane in the 20–60 GHz range.

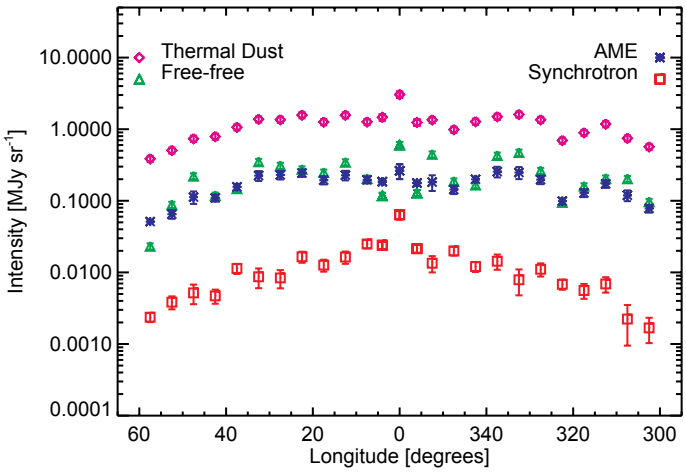

Fig. 11. Longitude distribution of all four components derived from SEDs and component separation, in 5° longitude intervals. The thermal dust is at 545 GHz scaled down by a factor of 100. The free-free, AME, and synchrotron, have been scaled to 28.4 GHz. The conversion factor from intensity to brightness temperature at 28.4 GHz is 40 mK MJy^{-1} sr.

6.5. The longitude distribution of the four components

Figure 5 shows the longitude distribution of the total emission at b = 0° for illustrative frequencies. The emission is smoothed to 1° resolution and includes the diffuse, broader latitude emission as well as point sources. The total emission is strongest in the inner Galaxy for l = 300° → 0° → 60° where it is 5–10 times that at l = 80°–90°or l = 270°–280°. Individual features in the local spiral arm can be seen in all four emission components at l = 73°–85° (Cygnus X) and l = 282°–295°.

In order to give an overview of the longitude distribution of each of the four emission components, the intensities are derived for longitude intervals of 5°. This interval also gives a robust SED from which to separate the components. Figure 11 shows the distribution of the four emission components at b = 0° at l = 300° → 0° → 60° averaged over 5° intervals in longitude.

Table 9. Intrinsic latitude widths of various Galactic components.

Component	Width
OB stars (Wood & Churchwell 1989)	$0.^{\circ}83 \pm 0.^{\circ}05$
Dense CS clouds (Bronfman et al. 2000)	$0.^{\circ}90 \pm 0.^{\circ}05$
Free-free via RRLs (n_e^2)	$0.^{\circ}92 \pm 0.^{\circ}05$
Free-free from FastMEM	$1.^{\circ}07 \pm 0.^{\circ}05$
CO	$1.^{\circ}19 \pm 0.^{\circ}08$
Dust – FIR (100 μm)	$1.^{\circ}24 \pm 0.^{\circ}02$
Planck 353, 545, 857 GHz	$1.^{\circ}30 \pm 0.^{\circ}04$
Gamma-rays (representative of total matter)	$1.^{\circ}26 \pm 0.^{\circ}05$
Synchrotron, GHz frequencies	$1.^{\circ}65 \pm 0.^{\circ}05$
Synchrotron, *K*-band polarization	$1.^{\circ}67 \pm 0.^{\circ}13$
Neutral hydrogen	$1.^{\circ}98 \pm 0.^{\circ}05$

Notes. The widths are the mean values in the longitude range $l = 330°$–$340°$, $l = 20°$–$30°$, and $l = 30°$–$40°$. Values in the 320°–330° range are a factor of $\sim 1.35 \pm 0.05$ greater.

The synchrotron emission is given by the 408 MHz emission corrected by free-free; this correction is typically 20% on the plane (Alves et al. 2012). The free-free emission is estimated from RRL data and the FastMEM analysis. The thermal dust indicator is the *Planck* 545 GHz emission, which is not contaminated by the other emission components. The AME emission is the residual when the other three components are subtracted from the total emission. For ease of comparison in Fig. 11, the synchrotron, free-free, and AME are evaluated at 28.4 GHz, which is close to the peak of the AME emission.

The longitude distributions of the four emission components shown in Fig. 11 are broadly similar, as might be expected from Fig. 5. The highest rate of star formation is occurring in the inner two spiral arms of the Galaxy (Bronfman et al. 2000; Wood & Churchwell 1989; Alves et al. 2012). The velocities of the gaseous components show that the inner arms located between $R_G = 4$ to 6.5 kpc are responsible. We note the increase in emission of all components towards the Galactic centre; the spiral arms are not differentiated because of the 5° smoothing and the use of a logarithmic scale. The outer arms sampled at $l = 270°$–$300°$ and at $l = 60°$–$90°$ are a factor of 3–4 less bright than the inner arms. The inference from Fig. 11 is that all four components studied here are tightly related to current star formation.

7. Discussion and conclusions

We have identified four components of emission within the inner Galaxy that are narrow in Galactic latitude; their emission extends over the whole frequency range of *Planck* and into the radio, FIR, and gamma-ray regions. Their longitude distribution is similar in all these bands, and indicates that this emission originates within the inner spiral arms, principally the Carina-Sagittarius arm and the Norma-Scutum arm, as shown in Figs. 3 and 5 and discussed in Sect. 5.2. The FWHM width in the range 1° to 2° of the various components corresponds to a FWHM z-thickness of 100 to 200 pc at the distance of the spiral arms. A principal result relating to Galactic structure is the difference in latitude width of the various emission components. These differences reflect the different formation processes and life-histories of the components. The FWHM data are summarized in Table 9.

7.1. Free-free

The free-free emission is determined by RRL observations in the range $l = 20°$–$44°$ and by a FastMEM analysis over the rest of the range, $l = 300° \rightarrow 0° \rightarrow 60°$. Free-free is the narrowest of the four components with a typical FWHM of $1.^{\circ}06 \pm 0.^{\circ}05$, which is wider than that of the recently formed OB stars ($FWHM = 0.^{\circ}83 \pm 0.^{\circ}05$; Wood & Churchwell 1989) and dense molecular clouds ($FWHM = 0.^{\circ}90 \pm 0.^{\circ}05$; Bronfman et al. 2000) but narrower than H I ($1.^{\circ}98 \pm 0.^{\circ}05$), FIR dust ($1.^{\circ}24 \pm 0.^{\circ}02$), and the *Planck* dust ($1.^{\circ}30 \pm 0.^{\circ}04$). This narrowing of the young stellar population distribution relative to that of the gas is a consequence of the star formation rate being a nonlinear function of gas density – normally taken as proportional to n_H^2. This process naturally narrows the latitude distribution of the young stars relative to that of the gas and dust. Similarly the free-free latitude distribution will be narrower than that of the gas and dust since the free-free brightness is proportional to the EM ($n_e^2 l$).

7.2. Synchrotron

The synchrotron study has identified a narrow latitude distribution with $FWHM = 1.^{\circ}7$, which is superposed on a broader Galactic halo distribution of $FWHM \sim 10°$, as shown in Figs. 1 and 2. At 408 MHz these two distributions have similar brightness temperatures at $b = 0°$ in the inner Galaxy. The synchrotron emission reflects the current CRE distribution, modified by the local magnetic field B as $B^{1.7}$–$B^{2.0}$ (Strong et al. 2011) for the range of spectral indices considered here. These observations suggest the following scenario. The OB star population produces SNe in a narrow distribution on the plane. These SNe are the source of the CREs. As the SNRs expand over their 10^5–10^6 yr lifetime, the CREs continue to produce synchrotron emission in the magnetic fields of the decaying remnants. Other CREs escape from the SNRs and radiate in the ordered magnetic field of the plane. This ordered magnetic field in the inner Galaxy produces the narrow band of highly (30–50%) polarized emission on the plane seen in the WMAP K, Ka, and Q bands, which is a further justification for identifying this narrow band as a separate synchrotron component. In contrast, the synchrotron polarization at latitudes $|b| = 2°$–$5°$ is markedly lower at a level of 5–10%, presumably as a result of the tangled structures seen in the WMAP polarization maps.

Related information comes from the SNR and pulsar latitude distributions. The latitude distribution of SNRs in the Green (2009) catalogue has a FWHM of ~1.0°, very similar to that of the parent OB star population. Normal pulsars (neutron stars) formed in the SN event also have lifetimes of 10^5–10^6 yr and have proper motions with a component perpendicular to the plane of ~200 km s^{-1}. In the pulsar lifetime they will have travelled ~100 pc giving a FWHM of ~2° at a distance of 6 kpc, a value consistent with observation (Fig. 7, Table 4) again significantly broader than the OB star distribution. Pulsar and OB star data indicate that the current SN rate for our Galaxy is 2–4 per century (Keane & Kramer 2008; Wood & Churchwell 1989); this would imply ~6000 pulsars and SNRs on or near the Galactic plane with ages up to ~10^5 years. These SNRs could make a significant contribution to the narrow distribution on the plane and provide the disordered magnetic field at intermediate latitudes seen in WMAP polarization data.

7.3. AME

AME is clearly identified in the SED analysis where the *Planck* data define the high frequency side of the expected peaked spectrum (Draine & Lazarian 1998a). The AME emission is the main emission component on the plane along with free-free emission

over the frequency range 20−70 GHz. Above 70 GHz thermal dust becomes a significant contributor. The ratio AME/free-free for the diffuse emission on the Galactic plane is of interest for comparison with that of individual H II regions. The longitude distributions of both AME and free-free in Fig. 11 indicate that there is an overall correlation between them. The weighted average value of AME/free-free for the longitude range $l = 300° \rightarrow 0° \rightarrow 60°$ is 0.75 ± 0.03 as measured at 28.4 GHz (see Table 8). There appears to be a marginally significant increase in the ratio between the innermost (0.71 ± 0.04) and the outer (0.80 ± 0.04) regions of the inner Galaxy. There is a similar increase in the ratio of AME to 100 μm dust emission (7.1 ± 0.4 to 9.8 ± 0.5 mK MJy^{-1} sr; see Table 8). These values may be compared with other estimates of AME in the total emission at 28.4 GHz: Planck Collaboration Int. XV (2014) found the average AME fraction to be 0.50 ± 0.02 for individual bright AME regions, compared with the average value of 0.45 ± 0.01 found here for the combination of $l = 5°$–$60°$ and $300°$–$355°$. Planck Collaboration XXI (2011) found an average spinning dust fraction of 25 ± 5% at 30 GHz. This discrepancy can be explained by the fact that their value represents the average over all longitudes, with higher values found in the inner galaxy. Also, the uncertainties are likely to be under-estimated due to modelling errors.

Several investigations have shown that the dust emissivity index $\beta_{\rm dust}$ appears to vary with frequency, flattening in the millimetre range relative to the best single greybody fit, and also with environment (Reach et al. 1995; Finkbeiner et al. 1999; Galliano et al. 2005; Paladini et al. 2007; Planck Collaboration XVII 2011; Planck Collaboration Int. XIV 2014). We find that a single-$\beta_{\rm dust}$ fit to the dust spectrum changes the AME component at 28.4 GHz by ≤1%.

7.4. Thermal dust

There is an indication that the dust brightness has different latitude widths in different frequency ranges. The cooler dust at HFI frequencies (143−857 GHz) has a FWHM width of $1\overset{\circ}{.}30 \pm 0\overset{\circ}{.}04$, while the warmer dust at the shortest IRAS wavelength (12 μm) has a width of $1\overset{\circ}{.}44 \pm 0\overset{\circ}{.}03$. Both these values of dust width are less than that of the H I, which is $1\overset{\circ}{.}98 \pm 0\overset{\circ}{.}05$ (average of values in Table 5). Heating of the dust nearer the OB-stars would give a higher dust temperature and hence higher brightness temperature near the plane, leading to a narrower width. Our SED analysis gives estimates of the dust temperature and spectral index for the narrow inner Galaxy component. The dust latitude distribution is wider than that of the OB-stars heating the dust. We have determined values of dust parameters in the 1° FWHM beam on the Galactic plane for $l = 320°$–$340°$ and $l = 20°$–$40°$. We find mean values of $T_{\rm dust} = 20.4 \pm 0.4$ K, $\beta_{\rm FIR} = 1.94 \pm 0.03$, and $\beta_{\rm mm} = 1.67 \pm 0.02$. These values are in close agreement with those determined by Planck Collaboration Int. XIV (2014) for the $l = 20°$–$44°$ and $|b| < 1°$ region.

7.5. Application to other galaxies

The results obtained here for the inner Galactic plane can be compared with the integrated data for similar spiral galaxies. The high levels of AME and free-free relative to synchrotron found at 20−40 GHz for the inner Galaxy contrast with the ratios found for the integrated emission in spiral galaxies (Niklas et al. 1997; Peel et al. 2011). This could be because the equivalent of the narrow inner galaxy studied here is only a fraction of the total emission volume of the Galaxy, with the broader halo synchrotron components contributing the major part of the total emission. Data for 74 normal galaxies studied by Niklas et al. (1997) have an average ratio of free-free to synchrotron flux density of 0.08 ± 0.01 at 1.0 GHz; this translates to a ratio at 28.4 GHz of 0.99, assuming a synchrotron flux density spectral index of −0.83 at 1−10 GHz and −1.0 at higher frequencies. We find a free-free to synchrotron ratio of ∼ 30 at 28.4 GHz for the narrow component as shown in Fig. 9. This factor of 30 difference in the ratio can be accounted for by the larger synchrotron volume of the total galaxy as compared with the narrow inner Galaxy (a factor of ∼15 in latitude as shown in Figs. 1, 2 and 4 and ∼ 2 in longitude). Total-power high-resolution measurements of edge-on galaxies (tilt within 2°–5°) over a wide range of frequencies would be decisive in showing the presence or otherwise of such a narrow component at each of the four emission mechanisms in normal spiral galaxies.

Acknowledgements. We acknowledge the use of the Legacy Archive for Microwave Background Data Analysis (LAMBDA); support for LAMBDA is provided by the NASA Office of Space Science. Some of the results in this paper have been derived using the HEALPix package The development of *Planck* has been supported by: ESA; CNES and CNRS/INSU-IN2P3-INP (France); ASI, CNR, and INAF (Italy); NASA and DoE (USA); STFC and UKSA (UK); CSIC, MICINN, JA and RES (Spain); Tekes, AoF and CSC (Finland); DLR and MPG (Germany); CSA (Canada); DTU Space (Denmark); SER/SSO (Switzerland); RCN (Norway); SFI (Ireland); FCT/MCTES (Portugal); and PRACE (EU). The research leading to these results has received funding from an STFC Consolidated Grant (No. ST/L000768/1), as well as the European Research Council under the European Union's Seventh Framework Programme (FP7/2007-2013)/ERC grant agreement Nos. 267934 and 307209. A description of the Planck Collaboration and a list of its members, including the technical or scientific activities in which they have been involved, can be found at `http://www.sciops.esa.int/index.php?project=planck&page=Planck_Collaboration`.

References

Abdo, A. A., Ackermann, M., Ajello, M., et al. 2010a, ApJ, 710, L92
Abdo, A. A., Ackermann, M., Ajello, M., et al. 2010b, ApJ, 708, 1254
Abdo, A. A., Ackermann, M., Ajello, M., et al. 2010c, Phys. Rev. Lett., 104, 101101
Abdo, A. A., Ackermann, M., Ajello, M., et al. 2010d, ApJ, 722, 1303
Ackermann, M., Ajello, M., Baldini, L., et al. 2011, ApJ, 726, 81
Ackermann, M., Ajello, M., Albert, A., et al. 2012, ApJS, 203, 4
Ali-Haïmoud, Y., Hirata, C. M., & Dickinson, C. 2009, MNRAS, 395, 1055
Alves, M. I. R., Davies, R. D., Dickinson, C., et al. 2010, MNRAS, 405, 1654
Alves, M. I. R., Davies, R. D., Dickinson, C., et al. 2012, MNRAS, 422, 2429
Atwood, W. B., Abdo, A. A., Ackermann, M., et al. 2009, ApJ, 697, 1071
Banday, A. J., Dickinson, C., Davies, R. D., Davis, R. J., & Górski, K. M. 2003, MNRAS, 345, 897
Bania, T. M., Anderson, L. D., Balser, D. S., & Rood, R. T. 2010, ApJ, 718, L106
Beichman, C. A., Neugebauer, G., Habing, H. J., Clegg, P. E., & Chester, T. J. 1988, Infrared astronomical satellite (IRAS) catalogs and atlases, Explanatory supplement, 1
Bennett, C. L., Smoot, G. F., Hinshaw, G., et al. 1992, ApJ, 396, L7
Bennett, C. L., Hill, R. S., Hinshaw, G., et al. 2003, ApJS, 148, 97
Bennett, C. L., Larson, D., Weiland, J. L., et al. 2013, ApJS, 208, 20
Berkhuijsen, E. M., & Müller, P. 2008, A&A, 490, 179
Berkhuijsen, E. M., Mitra, D., & Mueller, P. 2006, Astron. Nachr., 327, 82
Bersanelli, M., Mandolesi, N., Butler, R. C., et al. 2010, A&A, 520, A4
Beuermann, K., Kanbach, G., & Berkhuijsen, E. M. 1985, A&A, 153, 17
Blandford, R. D., & Ostriker, J. P. 1978, ApJ, 221, L29
Bonaldi, A., Bedini, L., Salerno, E., Baccigalupi, C., & de Zotti, G. 2006, MNRAS, 373, 271
Brandt, T. D., & Draine, B. T. 2012, ApJ, 744, 129
Broadbent, A., Osborne, J. L., & Haslam, C. G. T. 1989, MNRAS, 237, 381
Bronfman, L., Casassus, S., May, J., & Nyman, L.-Å. 2000, A&A, 358, 521
Casassus, S., Dickinson, C., Cleary, K., et al. 2008, MNRAS, 391, 1075
Chatterjee, S., Brisken, W. F., Vlemmings, W. H. T., et al. 2009, ApJ, 698, 250
Clemens, D. P. 1985, ApJ, 295, 422
Cohen, R. J., & Davies, R. D. 1976, MNRAS, 175, 1
Cordes, J. M., & Lazio, T. J. W. 2002, ArXiv e-prints [`arXiv:astro-ph/0207156`]

Cordes, J. M., & Lazio, T. J. W. 2003, ArXiv e-prints [arXiv:astro-ph/0301598]
Dame, T. M., Hartmann, D., & Thaddeus, P. 2001, ApJ, 547, 792
Davies, R. D., Dickinson, C., Banday, A. J., et al. 2006, MNRAS, 370, 1125
de Oliveira-Costa, A., Tegmark, M., Gutierrez, C. M., et al. 1999, ApJ, 527, L9
Delabrouille, J., Betoule, M., Melin, J.-B., et al. 2013, A&A, 553, A96
Delahaye, T., Lavalle, J., Lineros, R., Donato, F., & Fornengo, N. 2010, A&A, 524, A51
Dennison, B., Simonetti, J. H., & Topasna, G. A. 1998, PASA, 15, 147
Désert, F., Boulanger, F., & Puget, J. L. 1990, A&A, 237, 215
Dickey, J. M., & Lockman, F. J. 1990, ARA&A, 28, 215
Dickey, J. M., Strasser, S., Gaensler, B. M., et al. 2009, ApJ, 693, 1250
Dickinson, C. 2013, Adv. Astron., 2013, 4
Dickinson, C., Davies, R. D., & Davis, R. J. 2003, MNRAS, 341, 369
Dobler, G. 2012, ApJ, 760, L8
Dobler, G., Draine, B., & Finkbeiner, D. P. 2009, ApJ, 699, 1374
Dobler, G., Finkbeiner, D. P., Cholis, I., Slatyer, T., & Weiner, N. 2010, ApJ, 717, 825
Draine, B. T. 2011, Physics of the Interstellar and Intergalactic Medium (Princeton University Press)
Draine, B. T., & Lazarian, A. 1998a, ApJ, 494, L19
Draine, B. T., & Lazarian, A. 1998b, ApJ, 508, 157
Dunkley, J., Komatsu, E., Nolta, M. R., et al. 2009a, ApJS, 180, 306
Dunkley, J., Spergel, D. N., Komatsu, E., et al. 2009b, ApJ, 701, 1804
Finkbeiner, D. P. 2004, ApJ, 614, 186
Finkbeiner, D. P., Davis, M., & Schlegel, D. J. 1999, ApJ, 524, 867
Gaensler, B. M., Madsen, G. J., Chatterjee, S., & Mao, S. A. 2008, PASA, 25, 184
Galliano, F., Madden, S. C., Jones, A. P., Wilson, C. D., & Bernard, J.-P. 2005, A&A, 434, 867
Galliano, F., Hony, S., Bernard, J.-P., et al. 2011, A&A, 536, A88
Gaustad, J. E., McCullough, P. R., Rosing, W., & Van Buren, D. 2001, PASP, 113, 1326
Ghosh, T., Banday, A. J., Jaffe, T., et al. 2012, MNRAS, 422, 3617
Gold, B., Bennett, C. L., Hill, R. S., et al. 2009, ApJS, 180, 265
Gold, B., Odegard, N., Weiland, J. L., et al. 2011, ApJS, 192, 15
Gordon, M. A., & Sorochenko, R. L., eds. 1990, Radio recombination lines: 25 years of investigation (Dordrecht: Kluwer), Astrophys. Space Sci. Libr., 163
Gordon, K. D., Galliano, F., Hony, S., et al. 2010, A&A, 518, L89
Górski, K. M., Hivon, E., Banday, A. J., et al. 2005, ApJ, 622, 759
Green, D. A. 2009, Bull. Astron. Soc. India, 37, 45
Grenier, I. A., Casandjian, J.-M., & Terrier, R. 2005, Science, 307, 1292
Hart, L., & Pedlar, A. 1976, MNRAS, 176, 547
Hartmann, D., & Burton, W. B. 1997, Atlas of Galactic Neutral Hydrogen (Cambridge: Cambridge University Press)
Haslam, C. G. T., Salter, C. J., Stoffel, H., & Wilson, W. E. 1982, A&AS, 47, 1
Hauser, M. G., Arendt, R. G., Kelsall, T., et al. 1998, ApJ, 508, 25
Hoang, T., Lazarian, A., & Draine, B. T. 2011, ApJ, 741, 87
Hobson, M. P., Jones, A. W., Lasenby, A. N., & Bouchet, F. R. 1998, MNRAS, 300, 1
Hurier, G., Macías-Pérez, J. F., & Hildebrandt, S. 2013, A&A, 558, A118
Jaffe, T. R., Banday, A. J., Leahy, J. P., Leach, S., & Strong, A. W. 2011, MNRAS, 416, 1152
Jonas, J. L., Baart, E. E., & Nicolson, G. D. 1998, MNRAS, 297, 977
Kalberla, P. M. W., & Kerp, J. 2009, ARA&A, 47, 27
Keane, E. F., & Kramer, M. 2008, MNRAS, 391, 2009
Kogut, A., Banday, A. J., Bennett, C. L., et al. 1996, ApJ, 464, L5
Kogut, A., Dunkley, J., Bennett, C. L., et al. 2007, ApJ, 665, 355
Kogut, A., Fixsen, D. J., Levin, S. M., et al. 2011, ApJ, 734, 4
Kurtz, S. 2002, in Hot Star Workshop III: The Earliest Phases of Massive Star Birth, ed. P. Crowther, ASP Conf. Ser., 267, 81
Lagache, G. 2003, A&A, 405, 813
Lamarre, J., Puget, J., Ade, P. A. R., et al. 2010, A&A, 520, A9
Lawson, K. D., Mayer, C. J., Osborne, J. L., & Parkinson, M. L. 1987, MNRAS, 225, 307
Leahy, J. P., Bersanelli, M., D'Arcangelo, O., et al. 2010, A&A, 520, A8
Lockman, F. J. 1976, ApJ, 209, 429
Lorimer, D. R., Faulkner, A. J., Lyne, A. G., et al. 2006, MNRAS, 372, 777
Macellari, N., Pierpaoli, E., Dickinson, C., & Vaillancourt, J. E. 2011, MNRAS, 418, 888
Manchester, R. N., Hobbs, G. B., Teoh, A., & Hobbs, M. 2005, AJ, 129, 1993
Mandolesi, N., Bersanelli, M., Butler, R. C., et al. 2010, A&A, 520, A3
Markwardt, C. B. 2009, in Astronomical Data Analysis Software and Systems XVIII, eds. D. A. Bohlender, D. Durand, & P. Dowler, ASP Conf. Ser., 411, 251
Mattila, K., Juvela, M., & Lehtinen, K. 2007, ApJ, 654, L131
Mennella, A., Butler, R. C., Curto, A., et al. 2011, A&A, 536, A3
Mertsch, P., & Sarkar, S. 2010, J. Cosmol. Astropart. Phys., 10, 019
Mertsch, P., & Sarkar, S. 2013, J. Cosmol. Astropart. Phys., 06, 041
Milne, D. K. 1971, in The Crab Nebula, eds. R. D. Davies, & F. Graham-Smith (Dordrecht: Reidel), IAU Symp., 46, 248
Miville-Deschênes, M., & Lagache, G. 2005, ApJS, 157, 302
Miville-Deschênes, M.-A., Ysard, N., Lavabre, A., et al. 2008, A&A, 490, 1093
Niklas, S., Klein, U., & Wielebinski, R. 1997, A&A, 322, 19
Orlando, E., & Strong, A. 2013, MNRAS, 436, 2127
Paladini, R., Burigana, C., Davies, R. D., et al. 2003, A&A, 397, 213
Paladini, R., Davies, R. D., & DeZotti, G. 2004, MNRAS, 347, 237
Paladini, R., Montier, L., Giard, M., et al. 2007, A&A, 465, 839
Paradis, D., Bernard, J.-P., & Mény, C. 2009, A&A, 506, 745
Paradis, D., Dobashi, K., Shimoikura, T., et al. 2012, A&A, 543, A103
Peel, M. W., Dickinson, C., Davies, R. D., Clements, D. L., & Beswick, R. J. 2011, MNRAS, 416, L99
Peel, M. W., Dickinson, C., Davies, R. D., et al. 2012, MNRAS, 424, 2676
Perrot, C. A., & Grenier, I. A. 2003, A&A, 404, 519
Phillipps, S., Kearsey, S., Osborne, J. L., Haslam, C. G. T., & Stoffel, H. 1981, A&A, 103, 405
Planck Collaboration 2011, The Explanatory Supplement to the Planck Early Release Compact Source Catalogue (ESA)
Planck Collaboration 2013, The Explanatory Supplement to the Planck 2013 results, http://pla.esac.esa.int/pla/index.html (ESA)
Planck Collaboration I. 2011, A&A, 536, A1
Planck Collaboration II. 2011, A&A, 536, A2
Planck Collaboration VII. 2011, A&A, 536, A7
Planck Collaboration VIII. 2011, A&A, 536, A8
Planck Collaboration IX. 2011, A&A, 536, A9
Planck Collaboration X. 2011, A&A, 536, A10
Planck Collaboration XI. 2011, A&A, 536, A11
Planck Collaboration XII. 2011, A&A, 536, A12
Planck Collaboration XIII. 2011, A&A, 536, A13
Planck Collaboration XIV. 2011, A&A, 536, A14
Planck Collaboration XV. 2011, A&A, 536, A15
Planck Collaboration XVI. 2011, A&A, 536, A16
Planck Collaboration XVII. 2011, A&A, 536, A17
Planck Collaboration XVIII. 2011, A&A, 536, A18
Planck Collaboration XIX. 2011, A&A, 536, A19
Planck Collaboration XX. 2011, A&A, 536, A20
Planck Collaboration XXI. 2011, A&A, 536, A21
Planck Collaboration XXII. 2011, A&A, 536, A22
Planck Collaboration XXIII. 2011, A&A, 536, A23
Planck Collaboration XXIV. 2011, A&A, 536, A24
Planck Collaboration XXV. 2011, A&A, 536, A25
Planck Collaboration I. 2014, A&A, 571, A1
Planck Collaboration XI. 2014, A&A, 571, A11
Planck Collaboration XIII. 2014, A&A, 571, A13
Planck Collaboration Int. IX. 2013, A&A, 554, A139
Planck Collaboration Int. XII. 2013, A&A, 557, A53
Planck Collaboration Int. XIV. 2014, A&A, 564, A45
Planck Collaboration Int. XV. 2014, A&A, 565, A103
Planck HFI Core Team 2011a, A&A, 536, A4
Planck HFI Core Team 2011b, A&A, 536, A6
Platania, P., Bensadoun, M., Bersanelli, M., et al. 1998, ApJ, 505, 473
Platania, P., Burigana, C., Maino, D., et al. 2003, A&A, 410, 847
Reach, W. T., Dwek, E., Fixsen, D. J., et al. 1995, ApJ, 451, 188
Reich, W. 1982, A&AS, 48, 219
Reich, P., & Reich, W. 1986, A&AS, 63, 205
Reich, P., & Reich, W. 1988, A&AS, 74, 7
Reich, P., Testori, J. C., & Reich, W. 2001, A&A, 376, 861
Reynolds, R. J., Tufte, S. L., Haffner, L. M., Jaehnig, K., & Percival, J. W. 1998, PASA, 15, 14
Rohlfs, K., & Wilson, T. L. 2004, Tools of radio astronomy (Berlin: Springer)
Rosset, C., Tristram, M., Ponthieu, N., et al. 2010, A&A, 520, A13
Rybicki, G. B., & Lightman, A. P. 1979, Radiative processes in astrophysics (New York: Wiley-Interscience)
Sandstrom, K. M., Bolatto, A. D., Draine, B. T., Bot, C., & Stanimirović, S. 2010, ApJ, 715, 701
Schnitzeler, D. H. F. M. 2012, MNRAS, 427, 664
Shaver, P. A. 1980, A&A, 90, 34
Shaver, P. A., McGee, R. X., Newton, L. M., Danks, A. C., & Pottasch, S. R. 1983, MNRAS, 204, 53
Stolyarov, V., Hobson, M. P., Ashdown, M. A. J., & Lasenby, A. N. 2002, MNRAS, 336, 97
Stolyarov, V., Hobson, M. P., Lasenby, A. N., & Barreiro, R. B. 2005, MNRAS, 357, 145
Strong, A. W. 2011, in Cosmic Rays for Particle and Astroparticle Physics, eds. S. Giani, C. Leroy, & P. G. Rancoita (Singapore: World Scientific Publishing), 473

Strong, A. W., Porter, T. A., Digel, S. W., et al. 2010, ApJ, 722, L58
Strong, A. W., Orlando, E., & Jaffe, T. R. 2011, A&A, 534, A54
Sun, X. H., Reich, W., Han, J. L., et al. 2011, A&A, 527, A74
Tauber, J. A., Mandolesi, N., Puget, J., et al. 2010, A&A, 520, A1
Tibbs, C. T., Watson, R. A., Dickinson, C., et al. 2010, MNRAS, 402, 1969
Tielens, A. G. G. M. 2008, ARA&A, 46, 289
Todorović, M., Davies, R. D., Dickinson, C., et al. 2010, MNRAS, 406, 1629
Watson, R. A., Rebolo, R., Rubiño-Martín, J. A., et al. 2005, ApJ, 624, L89
Witt, A. N., Gold, B., Barnes, F. S., et al. 2010, ApJ, 724, 1551
Wood, D. O. S., & Churchwell, E. 1989, ApJ, 340, 265
Ysard, N., & Verstraete, L. 2010, A&A, 509, A12
Ysard, N., Miville-Deschênes, M. A., & Verstraete, L. 2010, A&A, 509, L1
Zacchei, A., Maino, D., Baccigalupi, C., et al. 2011, A&A, 536, A5

[1] APC, AstroParticule et Cosmologie, Université Paris Diderot, CNRS/IN2P3, CEA/lrfu, Observatoire de Paris, Sorbonne Paris Cité, 10 rue Alice Domon et Léonie Duquet, 75205 Paris Cedex 13, France
[2] Aalto University Metsähovi Radio Observatory and Dept of Radio Science and Engineering, PO Box 13000, 00076 Aalto, Finland
[3] African Institute for Mathematical Sciences, 6-8 Melrose Road, Muizenberg, 7950 Cape Town, South Africa
[4] Agenzia Spaziale Italiana Science Data Center, via del Politecnico snc, 00133 Roma, Italy
[5] Agenzia Spaziale Italiana, viale Liegi 26, 00198 Roma, Italy
[6] Astrophysics Group, Cavendish Laboratory, University of Cambridge, J J Thomson Avenue, Cambridge CB3 0HE, UK
[7] Astrophysics & Cosmology Research Unit, School of Mathematics, Statistics & Computer Science, University of KwaZulu-Natal, Westville Campus, Private Bag X54001, 4000 Durban, South Africa
[8] Atacama Large Millimeter/submillimeter Array, ALMA Santiago Central Offices, Alonso de Cordova 3107, Vitacura, Casilla 763 0355, Santiago, Chile
[9] CITA, University of Toronto, 60 St. George St., Toronto, ON M5S 3H8, Canada
[10] CNRS, IRAP, 9 Av. colonel Roche, BP 44346, 31028 Toulouse Cedex 4, France
[11] California Institute of Technology, Pasadena, CA 91125 California, USA
[12] Computational Cosmology Center, Lawrence Berkeley National Laboratory, Berkeley, California 92093-0424, USA
[13] Consejo Superior de Investigaciones Científicas (CSIC), Madrid, Spain
[14] DSM/Irfu/SPP, CEA-Saclay, 91191 Gif-sur-Yvette Cedex, France
[15] DTU Space, National Space Institute, Technical University of Denmark, Elektrovej 327, 2800 Kgs. Lyngby, Denmark
[16] Département de Physique Théorique, Université de Genève, 24 Quai E. Ansermet,1211 Genève 4, Switzerland
[17] Departamento de Física Fundamental, Facultad de Ciencias, Universidad de Salamanca, 37008 Salamanca, Spain
[18] Departamento de Física, Universidad de Oviedo, Avda. Calvo Sotelo s/n, 33007 Oviedo, Spain
[19] Department of Astrophysics/IMAPP, Radboud University Nijmegen, PO Box 9010, 6500 GL Nijmegen, The Netherlands
[20] Department of Electrical Engineering and Computer Sciences, University of California, Berkeley, CA 94720-770 California, USA
[21] Department of Physics & Astronomy, University of British Columbia, 6224 Agricultural Road, Vancouver, British Columbia, BC V6T 1Z1, Canada
[22] Department of Physics and Astronomy, Dana and David Dornsife College of Letter, Arts and Sciences, University of Southern California, Los Angeles, CA 90089, USA
[23] Department of Physics and Astronomy, University College London, London WC1E 6BT, UK
[24] Department of Physics, Florida State University, Keen Physics Building, 77 Chieftan Way, Tallahassee, FL 32303 Florida, USA
[25] Department of Physics, Gustaf Hällströmin katu 2a, University of Helsinki, 00014 Helsinki, Finland
[26] Department of Physics, Princeton University, Princeton, New Jersey, NJ 08543-0451, USA
[27] Department of Physics, University of California, Santa Barbara, California, USA
[28] Department of Physics, University of Illinois at Urbana-Champaign, 1110 West Green Street, Urbana, Illinois, IL 61801-3080, USA
[29] Dipartimento di Fisica e Astronomia G. Galilei, Università degli Studi di Padova, via Marzolo 8, 35131 Padova, Italy
[30] Dipartimento di Fisica e Scienze della Terra, Università di Ferrara, via Saragat 1, 44122 Ferrara, Italy
[31] Dipartimento di Fisica, Università La Sapienza, P.le A. Moro 2, 00185 Roma, Italy
[32] Dipartimento di Fisica, Università degli Studi di Milano, via Celoria, 16, 20133 Milano, Italy
[33] Dipartimento di Fisica, Università degli Studi di Trieste, via A. Valerio 2, 34131 Trieste, Italy
[34] Dipartimento di Fisica, Università di Roma Tor Vergata, via della Ricerca Scientifica 1, 00133 Roma, Italy
[35] Discovery Center, Niels Bohr Institute, Blegdamsvej 17, 2100 Copenhagen, Denmark
[36] Dpto. Astrofísica, Universidad de La Laguna (ULL), 38206 La Laguna, Tenerife, Spain
[37] European Southern Observatory, ESO Vitacura, Alonso de Cordova 3107, Vitacura, Casilla 19001, Santiago, Chile
[38] European Space Agency, ESAC, Planck Science Office, Camino bajo del Castillo s/n, Urbanización Villafranca del Castillo, Villanueva de la Cañada, 28692 Madrid, Spain
[39] European Space Agency, ESTEC, Keplerlaan 1, 2201 AZ Noordwijk, The Netherlands
[40] Helsinki Institute of Physics, Gustaf Hällströmin katu 2, University of Helsinki, 00014 Helsinki, Finland
[41] INAF–Osservatorio Astronomico di Padova, Vicolo dell'Osservatorio 5, 35141 Padova, Italy
[42] INAF–Osservatorio Astronomico di Roma, via di Frascati 33, 00040 Monte Porzio Catone, Italy
[43] INAF–Osservatorio Astronomico di Trieste, via G.B. Tiepolo 11, 34131 Trieste, Italy
[44] INAF Istituto di Radioastronomia, via P. Gobetti 101, 40129 Bologna, Italy
[45] INAF/IASF Bologna, via Gobetti 101, 40129 Bologna, Italy
[46] INAF/IASF Milano, via E. Bassini 15, 20133 Milano, Italy
[47] INFN, Sezione di Bologna, via Irnerio 46, 40126, Bologna, Italy
[48] INFN, Sezione di Roma 1, Università di Roma Sapienza, Piazzale Aldo Moro 2, 00185, Roma, Italy
[49] INFN/National Institute for Nuclear Physics, via Valerio 2, 34127 Trieste, Italy
[50] IPAG: Institut de Planétologie et d'Astrophysique de Grenoble, Université Joseph Fourier, Grenoble 1 / CNRS-INSU, UMR 5274, 38041 Grenoble, France
[51] IUCAA, Post Bag 4, Ganeshkhind, Pune University Campus, Pune 411 007, India
[52] Imperial College London, Astrophysics group, Blackett Laboratory, Prince Consort Road, London, SW7 2AZ, UK
[53] Infrared Processing and Analysis Center, California Institute of Technology, Pasadena, CA 91125, USA
[54] Institut d'Astrophysique Spatiale, CNRS (UMR8617) Université Paris-Sud 11, Bâtiment 121, 91405 Orsay, France
[55] Institut d'Astrophysique de Paris, CNRS (UMR7095), 98bis boulevard Arago, 75014 Paris, France
[56] Institute for Space Sciences, 077125 Bucharest-Magurale, Romania
[57] Institute of Astronomy, University of Cambridge, Madingley Road, Cambridge CB3 0HA, UK
[58] Institute of Theoretical Astrophysics, University of Oslo, Blindern, Oslo, Norway
[59] Instituto de Astrofísica de Canarias, C/Vía Láctea s/n, La Laguna, 38200 Tenerife, Spain
[60] Instituto de Física de Cantabria (CSIC-Universidad de Cantabria), Avda. de los Castros s/n, 39005 Santander, Spain
[61] Jet Propulsion Laboratory, California Institute of Technology, 4800 Oak Grove Drive, Pasadena, CA 91109 California, USA

[62] Jodrell Bank Centre for Astrophysics, Alan Turing Building, School of Physics and Astronomy, The University of Manchester, Oxford Road, Manchester, M13 9PL, UK
[63] Kavli Institute for Cosmology Cambridge, Madingley Road, Cambridge, CB3 0HA, UK
[64] LAL, Université Paris-Sud, CNRS/IN2P3, 91898 Orsay, France
[65] LERMA, CNRS, Observatoire de Paris, 61 avenue de l'Observatoire, Paris, France
[66] Laboratoire AIM, IRFU/Service d'Astrophysique – CEA/DSM – CNRS – Université Paris Diderot, Bât. 709, CEA-Saclay, 91191 Gif-sur-Yvette Cedex, France
[67] Laboratoire Traitement et Communication de l'Information, CNRS (UMR 5141) and Télécom ParisTech, 46 rue Barrault, 75634 Paris Cedex 13, France
[68] Laboratoire de Physique Subatomique et de Cosmologie, Université Joseph Fourier Grenoble I, CNRS/IN2P3, Institut National Polytechnique de Grenoble, 53 rue des Martyrs, 38026 Grenoble Cedex, France
[69] Laboratoire de Physique Théorique, Université Paris-Sud 11 & CNRS, Bâtiment 210, 91405 Orsay, France
[70] Lawrence Berkeley National Laboratory, Berkeley, California CA 94720, USA
[71] Max-Planck-Institut für Astrophysik, Karl-Schwarzschild-Str. 1, 85741 Garching, Germany
[72] Max-Planck-Institut für Extraterrestrische Physik, Giessenbachstraße, 85748 Garching, Germany
[73] Max-Planck-Institut für Radioastronomie, Auf dem Hügel 69, 53121 Bonn, Germany
[74] MilliLab, VTT Technical Research Centre of Finland, Tietotie 3, 02044 Espoo, Finland
[75] National University of Ireland, Department of Experimental Physics, Maynooth, Co. Kildare, Ireland
[76] Niels Bohr Institute, Blegdamsvej 17, 2100 Copenhagen, Denmark
[77] Observational Cosmology, Mail Stop 367-17, California Institute of Technology, Pasadena, CA 91125, USA
[78] Optical Science Laboratory, University College London, Gower Street, London WC1E 6 BT, UK
[79] SISSA, Astrophysics Sector, via Bonomea 265, 34136, Trieste, Italy
[80] School of Physics and Astronomy, Cardiff University, Queens Buildings, The Parade, Cardiff, CF24 3AA, UK
[81] Special Astrophysical Observatory, Russian Academy of Sciences, Nizhnij Arkhyz, Zelenchukskiy region, Karachai-Cherkessian Republic, 369167, Russia
[82] UPMC Univ. Paris 06, UMR7095, 98bis Boulevard Arago, 75014 Paris, France
[83] Université de Toulouse, UPS-OMP, IRAP, 31028 Toulouse Cedex 4, France
[84] Universities Space Research Association, Stratospheric Observatory for Infrared Astronomy, MS 232-11, Moffett Field, CA 94035, USA
[85] University of Granada, Departamento de Física Teórica y del Cosmos, Facultad de Ciencias, 18071 Granada, Spain
[86] Warsaw University Observatory, Aleje Ujazdowskie 4, 00-478 Warszawa, Poland

Pages 25 to 27 are available in the electronic edition of the journal at http://www.aanda.org

Appendix A: Validation of FastMEM

A.1. Reconstruction of the free-free component using FastMEM

The Maximum Entropy Method (MEM) is used to separate the signals from cosmological and astrophysical foregrounds including CMB and Galactic foregrounds such as synchrotron, free-free, anomalous microwave emission (AME) and thermal dust. The implementation of MEM used here works in the spherical harmonic domain, where the separation is performed mode-by-mode allowing a huge optimization problem to be split into a number of smaller problems that can be done in parallel, saving CPU time. This approach, called FastMEM, is described by Hobson et al. (1998) for Fourier modes on flat patches of the sky and by Stolyarov et al. (2002) for the full-sky case.

The simulated data set used to check the quality of the recovery and reconstruction errors was the Full Focal Plane data set FFP4 (Planck Collaboration 2013). It includes all *Planck* frequency maps from 30 to 857 GHz properly simulated with plausible noise levels, systematics due to the scanning strategy, and real beam transfer functions. The components were modelled using the Planck Sky Model (PSM; Delabrouille et al. 2013) v1.7.

After multiple separation tests it was found that low-frequency components are very complicated to extract, especially AME. It was decided to use only the limited number of frequency maps, from 70.4 to 353 GHz. Since there were problems with WMAP modelled maps, they were not used in the analysis. However, WMAP data maps are essential for low-frequency component extraction from the real data.

The reconstructed components were CMB, thermal SZ, free-free, thermal dust, and CO $J = 1 \rightarrow 0$, $J = 2 \rightarrow 1$ and $J = 3 \rightarrow 2$ lines. It was assumed that AME and synchrotron contributions are very small in this range of frequencies. A small bias from the synchrotron component, however, could be possible in the Galactic plane. Free-free spectral scaling was calculated assuming average electron temperature $T_e = 6000\,\mathrm{K}$ (Alves et al. 2012).

The accuracy of the component separation was controlled in several ways. Firstly, the residuals between data maps and the modelled component contribution were calculated. There were component-free maps, containing only instrumental noise and point sources

$$\Delta T(\nu) = T(\nu)_{\rm data} - \hat{T}(\nu)_{\rm CMB} - \hat{T}(\nu)_{\rm dust} - \hat{T}(\nu)_{\rm ff} - \hat{T}(\nu)_{\rm SZt} - \hat{T}(\nu)_{\rm CO}, \quad (A.1)$$

and component-cleaned CMB maps at each frequency, containing CMB signal as well as receiver noise and point sources

$$T_{\rm CMB+noise+PS}(\nu) = T(\nu)_{\rm data} - \hat{T}(\nu)_{\rm dust} - \hat{T}(\nu)_{\rm ff} - \hat{T}(\nu)_{\rm SZt} - \hat{T}(\nu)_{\rm CO}. \quad (A.2)$$

To calculate residual maps one should smooth component models with the same beam, which is taken to be a Gaussian with $\theta_{\rm FWHM} = 13\farcm23$ at 70.4 GHz. Residual maps are shown on the Fig. A.1.

The reconstructed free-free map can be directly compared with the input template. The residual map shows that the reconstruction slightly overestimates the real free-free contribution in the Galactic plane (Fig. A.2), where the morphology is complex and includes many bright point sources.

It is also useful to consider the profiles of free-free emission along the Galactic plane, which are shown on the Fig. A.3, and T–T plots between input and reconstructed maps (Fig. A.4).

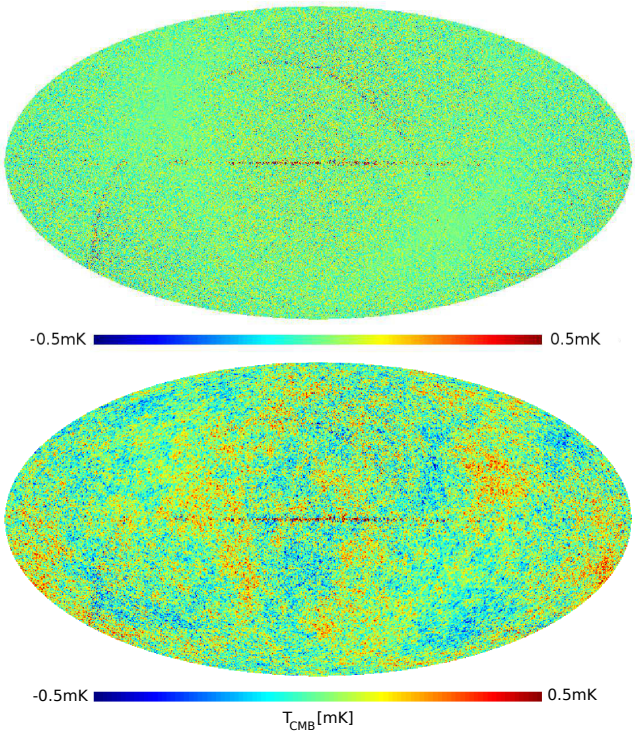

Fig. A.1. Simulated data: residual maps at 70.4 GHz, containing only receiver noise and point sources (Eq. (A.1), *upper panel*) and CMB component-cleaned map (Eq. (A.2), *lower panel*). The maps are in Mollweide projection, with $N_{\rm side} = 1024$ and a linear temperature scale with units of $T_{\rm CMB}$.

A.2. Comparison of free-free maps from FastMEM with other component separation methods

In this section we compare the free-free emission derived from FastMEM and other modelling methods with the direct measure of free-free using RRLs. In order to convert the RRL data to brightness temperature we have used an electron temperature, T_e, of 6000 K as found by Alves et al. (2012) for the Galactic plane region $l = 20°$–$44°$, $|b| \leq 4°$, which we also use for this comparison.

FastMEM was applied to *Planck* data in the frequency range 70.4–353 GHz and used to obtain the free-free, CO, and thermal dust components. The synchrotron component was assumed to be a small fraction of the total Galactic plane emission at these frequencies. This was tested by subtracting the synchrotron component found by Alves et al. (2012) with brightness temperature spectral indices in the range $\beta_{\rm synch} = -2.7$ to -3.1; the free-free component changed by $\leq 2\%$. Similarly, the effect of the AME component was minimal in the 70.4–353 GHz range. The AME amplitude was based on the 100 μm IRIS brightness and assuming 10 μK per MJy sr^{-1} at 30 GHz with a spectrum peaking at 20 GHz.

The WMAP 9-yr MEM free-free all-sky fit (Bennett et al. 2013) was used to map the $l = 20°$–$44°$, $|b| \leq 4°$ region of the Alves et al. (2012) RRL survey, which includes emission from the Sagittarius and Scutum spiral arms of the inner Galaxy. This fit is based on the WMAP frequency range 23–94 GHz and includes significant synchrotron and AME emission that could also be estimated separately.

The Correlated Component Analysis (CCA) component separation method (Bonaldi et al. 2006), as used in Planck Collaboration Int. XII (2013), was also applied to the RRL

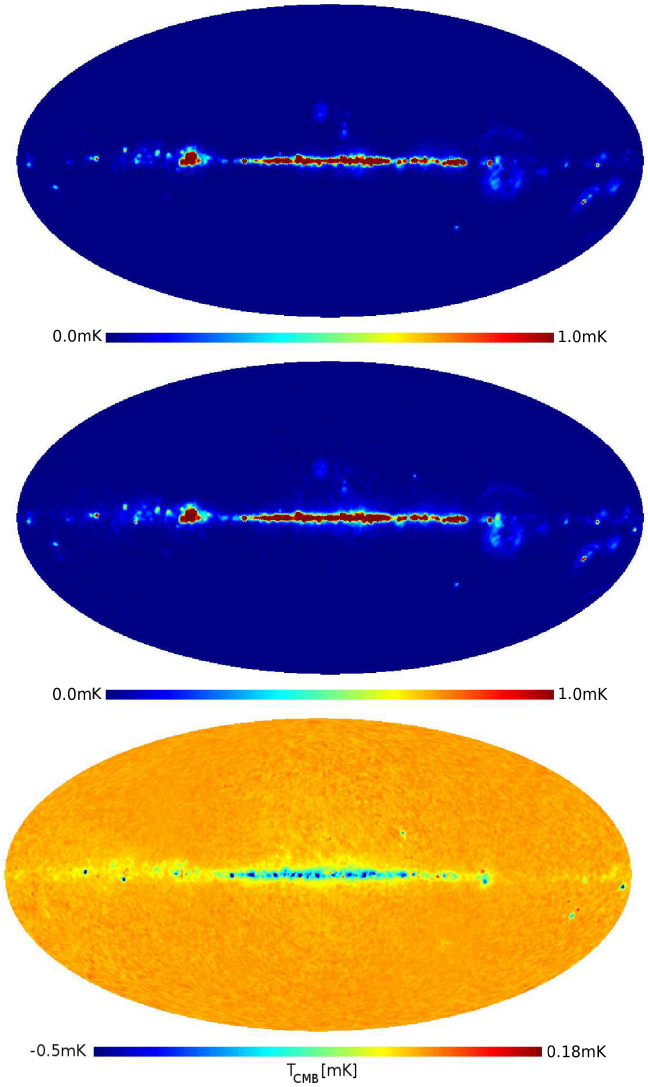

Fig. A.2. Input, reconstructed and residual maps of the free-free emission at 70.4 GHz. All maps are in Mollweide projection, smoothed with a 1° beam, $N_{side} = 128$. The colour scale is linear, and the units are mK_{CMB}.

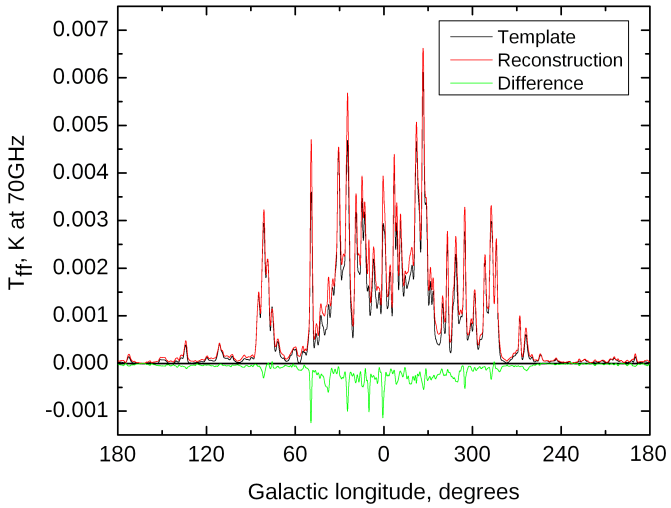

Fig. A.3. Input, reconstructed and residual Galactic plane profiles for the free-free emission at 70.4 GHz. Profiles were calculated over the maps shown in Fig. A.2; units are K_{CMB}. The plots are made for a 1°-resolution cut along the Galactic plane.

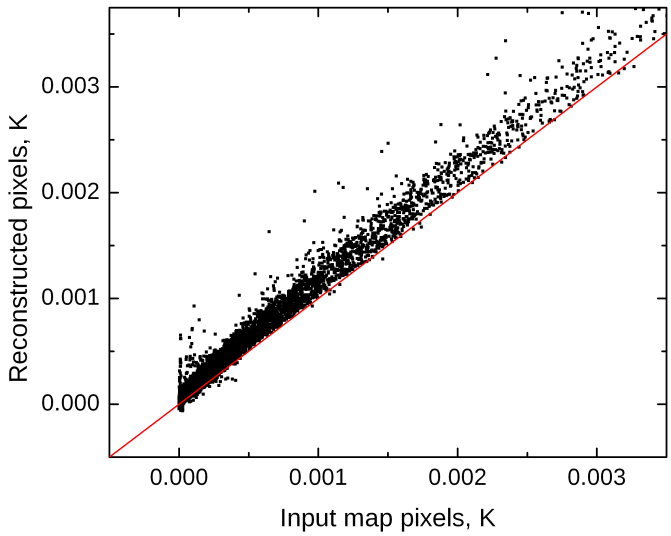

Fig. A.4. T–T plot comparing the pixel values in the simulated input map and in the reconstructed map. The solid red line indicates equality. The frequency is 70.4 GHz and the temperature scale is K_{CMB}.

region. The map of the free-free from RRLs is compared with those from FastMEM, WMAP9 MEM and CCA in Fig. A.5. The two MEM models and CCA are remarkably similar. The RRLs show the same structure but are somewhat weaker as we now show.

The T–T plots in Fig. A.6 show the relationships between the amplitudes of the RRL measurements and the three models. It can be seen that FastMEM from *Planck* and WMAP9 MEM agree closely. The CCA amplitudes are somewhat larger than the MEM solutions. The corresponding RRL amplitudes calculated for $T_e = 6000$ K are lower by ∼30%. The best fitting ratios of the slopes after removing offsets and including the brighter data only ($T_b \geq 0.3$ mK) are:

FastMEM/WMAP9 MEM	= 1.02
CCA/0.5 (FastMEM+WMAP9 MEM)	= 1.05
CCA/RRLs	= 1.35
0.5 (FastMEM + WMAP9 MEM)/RRLs	= 1.30.

We now consider what systematics could account for the difference between the RRL measurement and the three models, all of which agree within ∼5%. The assumption of $T_e = 6000$ K for the RRLs could be the source of part of the 30% difference. An increase of T_e from 6000 K to 7000 K for example would increase the free-free brightness temperature by 19%. On the other hand, the three models considered here each need to take account of the other foregrounds, which they do in different ways. This could possibly lead to an overestimate of the free-free emission if the other three spectral components were underestimates. We suggest that this difference may be resolved by using $T_e = 7000$ K and reducing the free-free component map by 10%.

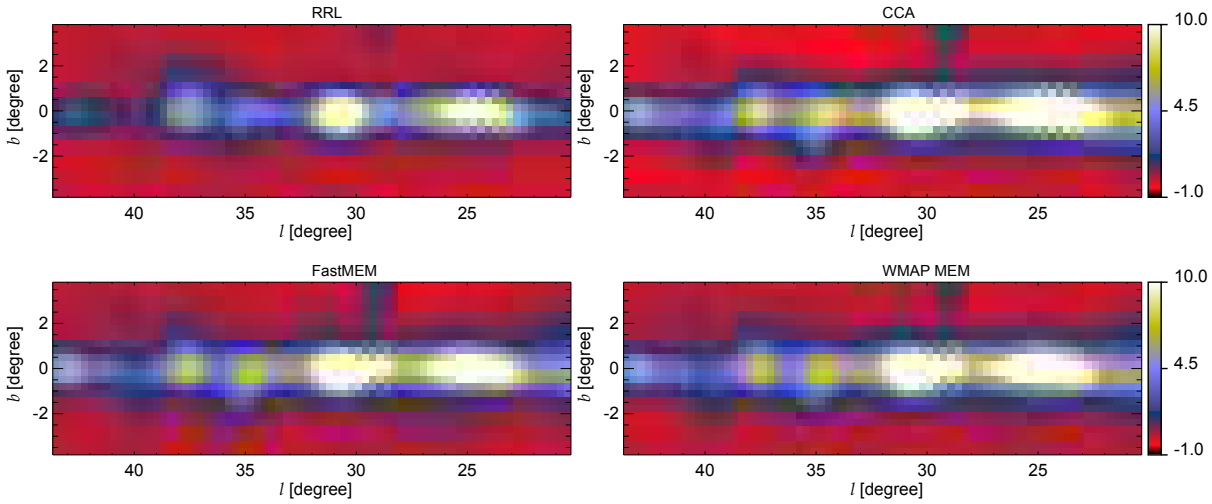

Fig. A.5. Maps of the $l = 20°–44°$, $b = -4°–+4°$ region of the inner Galaxy showing the free-free emission derived from RRLs, `FastMEM`, WMAP9 MEM, and CCA. The maps are at 33 GHz with 1° resolution and $N_{side} = 128$. The colour-coding is on a linear scale running from −1 to 10 mK_{RJ}.

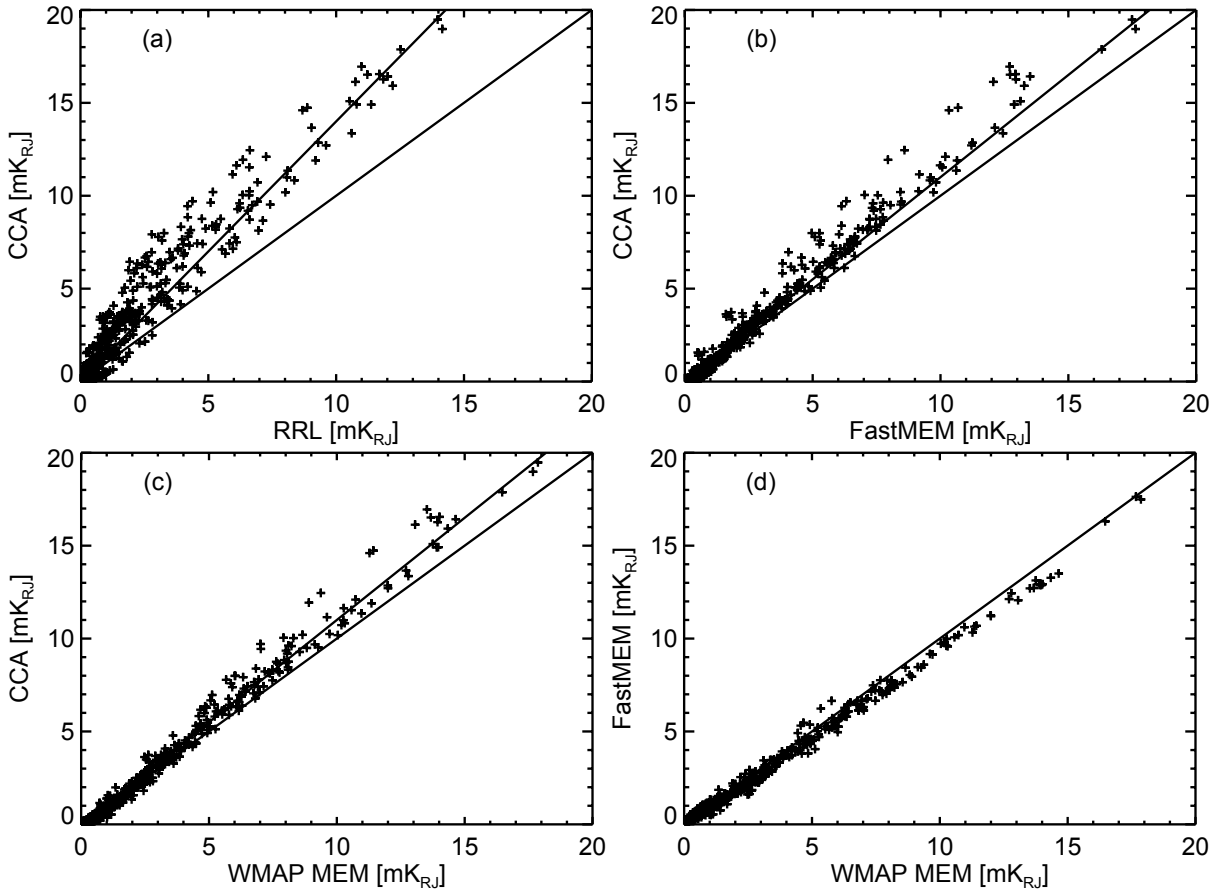

Fig. A.6. *T*–*T* plots comparing the free-free estimates from RRLs, WMAP9 MEM, and *Planck* data using `FastMEM` and CCA. The lower line indicates equality while the other line (where present) indicates the best fit. The frequency is 33 GHz and the resolution is 1°, with $N_{side} = 128$.